Poster ID: 3

B01

The 2025 International Workshop on the High Energy Circular Electron Positron Collider (CEPC2025), Guangzhou, China, Nov 5-10, 2025

Development of high voltage pulsed modulator for the CEPC C band 80MW Klystron

Fei Li[1] , Dayong He[1,2] , Jindong Liu[1,2] , Nan Gan[1,2], Yajie Mu[1] , Xiuqian Shi[1,2] , Zusheng Zhou[1.2†]

1Institute of High Energy Physics, Chinese Academy of Sciences, Beijing 100049

2University of Chinese Academy of Sciences, Beijing 100049, China

中国科学院高能物理研究所
Institute of High Energy Physics
Chinese Academy of Sciences

High-voltage pulse modulator is a key device in linear accelerators, serving as the intermediate link that converts power from the power supply into microwave power. According to the CEPC technical design, the linear accelerator requires 236 sets of C-band 80 MW power source systems to supply 5712 MHz/3 μs/100 Hz pulsed power to the accelerating structures. To achieve the target klystron output power of 80 MW, the high-voltage pulse modulator must deliver pulsed voltages of 425 kV, pulsed currents of 425 A, and a minimum output power of 180 MW. The pulse rise and fall times directly determine the modulator's efficiency, while repetition stability critically influences beam quality. The 100 Hz repetition rate imposes stringent requirements on power handling capacity and thermal management. To meet these challenges, a high-voltage pulse modulator based on a solid-state topology has been developed specifically for C-band 80 MW applications. This paper presents the current development progress from several aspects, including the comprehensive circuit calculation of the high-voltage pulse modulator, theoretical analysis and structural design of the pulse transformer, and simulation analysis.

INTRODUCTION

The structural layout of the CEPC Linac is shown in Fig.1. Its RF power source system consists of 33 sets of 80 MW pulsed klystrons operating at 2860 MHz (S-band) and 236 sets of 80 MW pulsed klystrons operating at 5720 MHz (C-band). Among them, each C-band 50 MW klystron supplies power to two 1.8 m accelerating structures, which operate at an accelerating gradient of 45 MV/m. To make the linac more compact, it is proposed to upgrade the C-band 50 MW klystrons to 80 MW klystrons. After the design is completed, a single 80 MW klystron can supply power to four 1.8 m accelerating structures, reducing the overall cost of the linac by approximately 30%. The fabrication of the C-band 80 MW klystrons started in October 2024, and high-power tests will be conducted by the end of 2025. The parameters of the C-band 50 MW/80MW klystron are presented in Table 1.

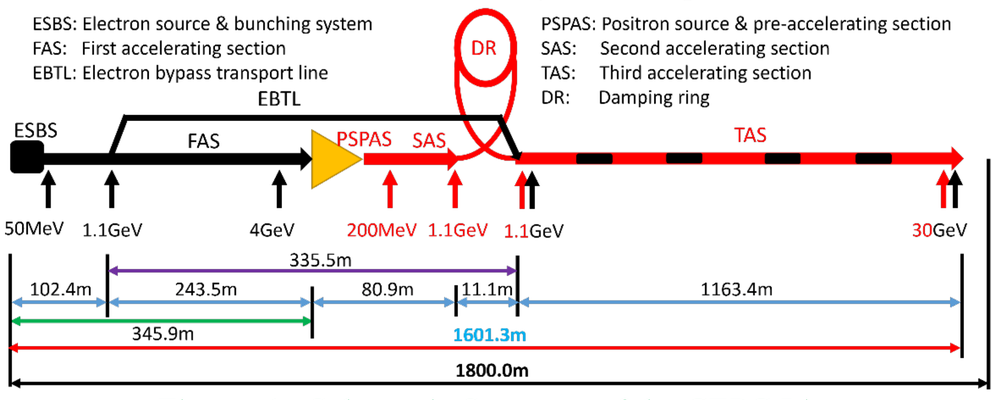

Figure. 1. Schematic Structure of the CEPC Linac.

Table. 1. Parameters of the C-band 50 MW/80MW Klystron

Parameters	**50 MWKlystron**	**80MW Klystron**
Output Power (MW)	50	80
Beam Voltage (kV)	350	425
Beam Current (A)	317	425
Efficiency (%)	48	47
Gain (dB)	＞50	＞50

SOLID-STATE MODULATOR

The high-voltage pulse modulator is a key device of the linear accelerator, acting as an intermediate link for converting electrical energy into microwave power. With the rapid iteration of solid-state power electronics technology, solid-state modulators featuring semiconductor devices as the core have demonstrated comprehensive advantages over the traditional PFN pulse power technology: they not only offer higher output stability and a more compact structure but also possess a much longer service life than thyratrons. This solid-state modulator consists of a high-precision direct current (DC) power supply, energy storage capacitors, IGBTs, low-inductance cables, and a matrix pulse transformer, whose schematic diagram is shown in Figure 2.

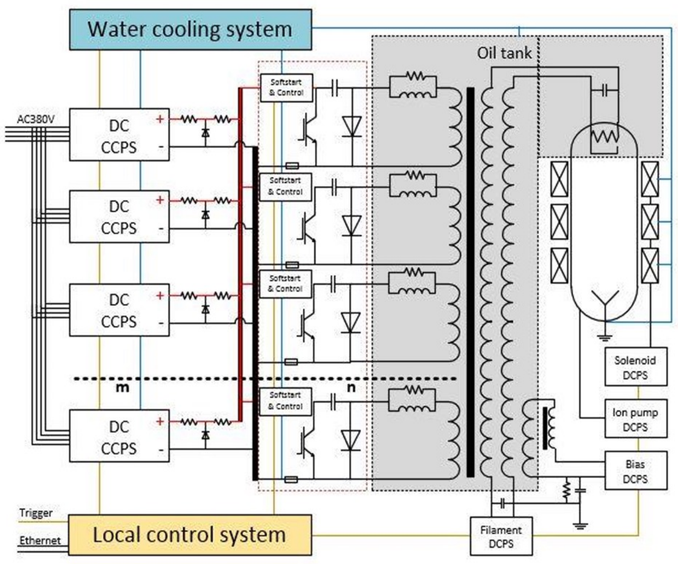

Figue.2. Schematic Diagram of the Solid-State Modulator.

Table. 2. Parameters of the C-band 80 MW Klystron

Parameters	**50 MWKlystron**
Pulse Voltage (kV)	430
Pulse Current (A)	440
Repetition Frequency (pps)	100
Pulse Width (μs)	3
Pulse Flat-Top Stability (%, within 4 μs)	1
Pulse Stability (%, over 3000 pulses)	0.02

For the C-band 5720 MHz/50 MW/100 pps/3 μs klystron load, the design parameters of its solid-state modulator are presented in Table 2. The solid-state modulator for the C-band 80 MW klystron has a pulse top width of 3 μs, a rise time and fall time of approximately 1.8 μs, resulting in a full width at half maximum (FWHM) of 4.4 μs for the pulse, and the average power of the DC power supply unit is 90.8 kW.

To ensure system redundancy, commercial 1,700 V IGBTs are adopted as switches for the discharge units, operating under the conditions of 1,000 V DC and 2,000 A. All discharge units work together, with a total current of 211 kA from 108 units. To control the pulse flatness within 1% over 3 μs, a parallel LR compensation circuit is specifically added to the discharge units. The pulse transformer of the solid-state modulator employs a biconical high-voltage winding to construct the DC current loop for the klystron cathode filament. The high-frequency characteristic $(L\delta/Cd)^{1/2}$ of the pulse transformer is determined by the leakage inductance Lδ and distributed capacitance Cd, which must be accurately matched to the impedance of the klystron.

REFERENCES

[1] The CEPC Study Group. CEPC Technical Design Report: Accelerator[J]. Radiation Detection Technology and Methods, 2024, 8(1).
[2] I. A. Guzilov, “BAC method of increasing the efficiency in klystrons”, s10th Int. Vacuum Elec. Sources Conf. (IVESC ’14), Saint Petersburg, Russia, July 2014.
[3] R. V. Egorov, I. A. Guzilov, “BAC-klystron: a new genera-tion of klystrons in vacuum electronics”, MOSCOW UNI-VERSITY PHYSICS BULLETIN, 2019, Vol. 74, No. 1, pp 38-42
[4] G. Burt et al., “Particle-in-cell simulation of a core stabiliza-tion method klystron”, IEEE International Vacuum Electronics Conference. (IVEC 2017), London, UK, April, 2017.
[5] IEEE Std 390TM-2007，IEEE Standard for Pulse Transformers.

*** Work supported by Yifang Wang’s Science Studio of the Thousand Talents Project**

† email address: zhouzs@ihep.ac.cn

Poster ID:10 The 2025 International Workshop on the High Energy Circular Electron Positron Collider (CEPC2025), Guangzhou , China, Nov 5-10, 2025

B02

Development of L-Band 10MW High Efficiency Multibeam Klystron

Noman Habib[1,2], Zu-Sheng Zhou[1,2*], Yu Liu[1,2], Ou-Zheng Xiao[1], Munawar Iqbal[1,3], Abid Aleem[1], Han Xiao[1,2], Yi-Ao Wang[1,2]

[1]Institute of High Energy Physics, Chinese Academy of Sciences, Beijing-China

[2]University of Chinese Academy of Sciences, Beijing-China

[3]Centre for High Energy Physics, University of the Punjab, Lahore-Pakistan

*Corresponding Author Email: zhouzs@ihep.ac.cn

Abstract

A complete 10 MW L-band multi-beam klystron has been designed and simulated for accelerator applications. At an acceleration potential of 115kV, a space-charge beam current of 130A is achieved, with an average cathode loading below 2.2A/cm². Calculations indicate that the maximum surface electric fields at the high-voltage ceramic seal and beam optics are under 1kV/mm and 6kV/mm, respectively. With an average beam radius of 6 mm, the electron beams are effectively transported to the interaction cavity, exhibiting a beam ripple of approximately 7%. Three-dimensional CST simulations confirm these results and show good agreement with 1D AJDISK, 2D-DGUN, 2D KLYC, 2D POISSON, and 2.5D EMSYS simulations.

Klystron Fundamentals

Definition: A multi-beam klystron (MBK) is an electron-beam vacuum tube in which multiple electron beams interact with standing-wave RF fields in several consecutive and collinear multi-tube RF cavities to generate high-power RF waves.

Mandate: It serves as the RF amplifier of an accelerator, providing the power needed to accelerate particles close to the speed of light.

Working Principle:

1.Electron Gun: The cathode is heated to approximately 1000 °C and biased with a pulsed or DC voltage of several hundred kilovolts. Electrons are accelerated from the cathode toward the grounded anode, which is electrically isolated from the cathode by high-voltage ceramics. The electron beams pass through the anode holes and drift along the drift tubes.

2. Magnet System: The electron beams are focused and guided using cathode coils, trim coils, and a solenoid.

3. RF Cavities: RF power applied to the input cavity velocity-modulates the electron beams.

On their path to the output cavity, the velocity modulation converts into density modulation via additional buncher cavities. In the output cavity, a negative electrode decelerates the electron beams. The energy lost by the electrons is converted into RF power.

4. RF Window: The generated RF power is extracted through a window and transmitted via a waveguide.

5 Collector: The residual electron beam is safely absorbed in the collector. Fig 1, is the cross-sectional view of the Klystron.

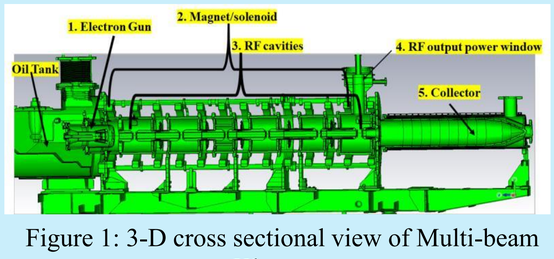

Figure 1: 3-D cross sectional view of Multi-beam Klystron.

Electron Gun Design

Table 1: Beam Optics Design Parameters

Parameters	Units	Values
Anode Diameter	mm	269.22
Focusing electrode diameter	mm	225.1
Cathode - anode spacing	mm	42.995
Cathode - focusing electrode spacing	mm	2
One of six cathodes diameter	mm	38

A 2D view of one of six cathodes & 3D view of the multi-beam Klystron electron gun shown in figure 2, was modeled in DGUN & CST Code with parameters given in table 1. This is a thermionic diode gun having cathode, focusing electrode and anode.

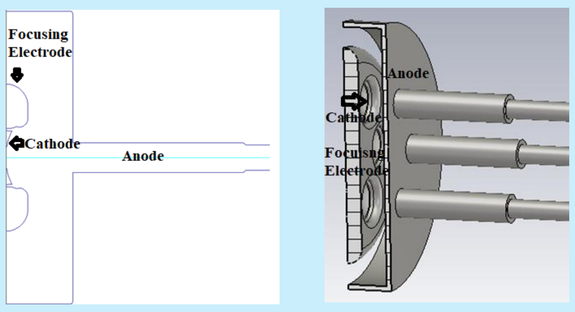

Figure 2: 2-D & 3-D model of the gun produced by DGUN &CST.

We used POISSON and CST code to design Gun envelope and calculate its electric field as shown below.

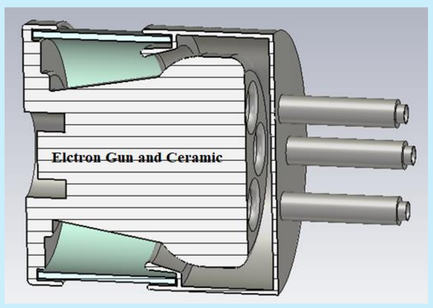

Figure 3: Design of the gun and ceramic in CST

We used POISSON and CST code to design solenoid as given in Fig. 4(a , b) with a Coil current at the cathode and trim coils for beam trajectories matching in the field free region. The obtained magnetic field in CST is given in Fig 5.

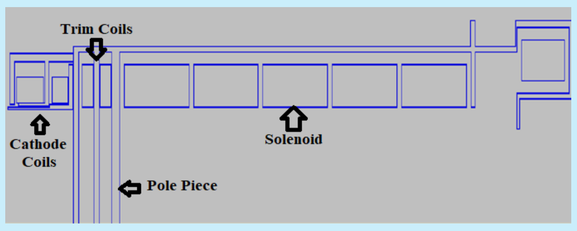

Figure 4a:Design of the solenoid in POISSON

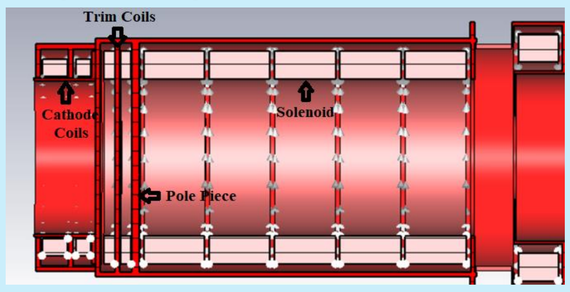

Figure 4b:Design of the solenoid in CST

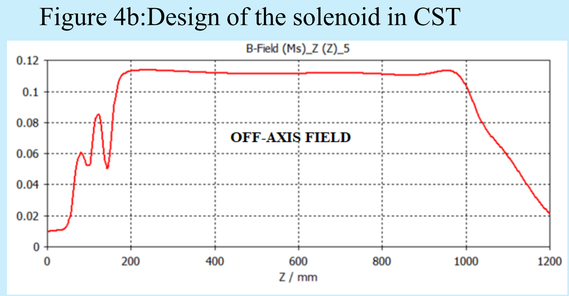

Figure 5:Axial Magnetic field profile of the Magnet(CST)

Beam Optics Simulation

Table 2. Simulation parameters

Parameter	Units	Values
Cathode voltage	kV	0
Anode voltage	kV	115
Magnetic field	Gauss	1058

The gun was then simulated in DGUN and CST Codes for the beam optics analysis. To get the maximum beam convergence, high emission density and low perveance in the field free region we used the parameters as listed in table2.

We obtained an electron beam of average radius of 6 mm in CST. The electron beams trajectories are shown in figure 6.

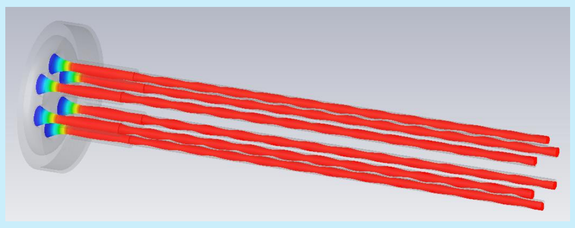

Figure 6: Beam trajectory of Multi-beam Klystron electron gun under magnetic field in CST

Beam Dynamic Simulation

Table 3. Simulation parameters

Cavity No.	R/Q	Qe	Qo	F(MHz)
1	138.052	479.874	10386.42	1300.396
2	132.013	8000	12358.61	1302.738
3	132.824	8000	10216.17	2585.419
4	132.099	8000	11545.00	1360.074
5	113.988	8000	10671.61	1352.017
6	123.585	46.929	10750.49	1296.552

We used AJDISK, KLYC, EMSYS and CST code to design Rf cavities by using the parameters given in the above table 3 and achieved the output power of more then 5MW from each port given in the table 3 and the beam trajectories are shown below in figure 7.

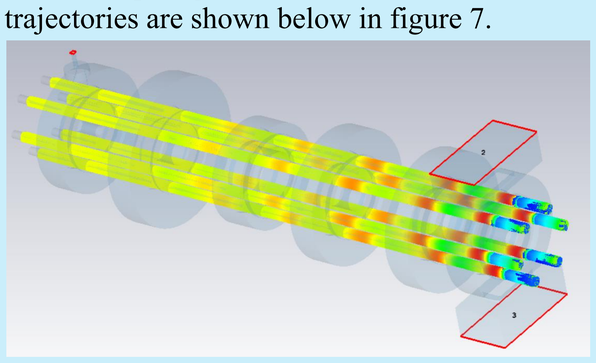

Figure 7: Beam trajectories of the RF structure in CST

Output windows

A 3D view of the multi-beam Klystron output window is shown in figure 8 below, was modeled in CST.

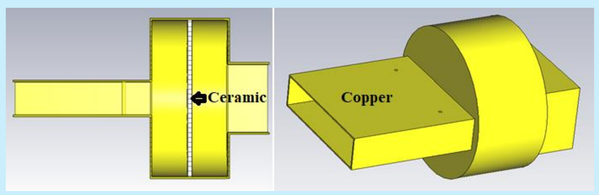

Figure 8: Design of the output window in CST

Results and Discussions

A maximum electric field value of 6 kV/mm at the focusing electrode is obtained as the potential lines are spaced very close to each other. A space charge current of one of 6 cathodes 21.8A is obtained as can be seen in the Figure 9. The perveance is calculated to be 3.3 μP.

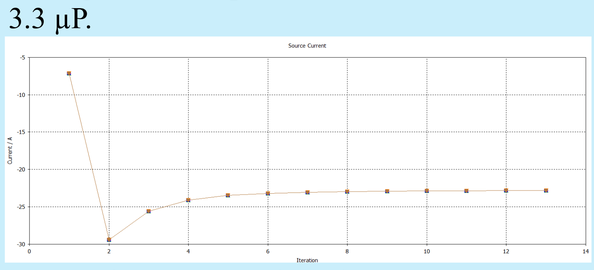

Figure 9: Space charge beam current

Figure 10 represents the graph which shows the output power from each port of the output cavity. The maximum value obtained is around 5.1 MW.

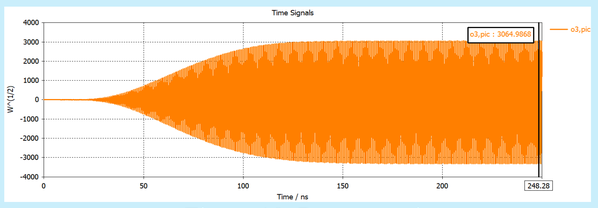

Figure 10: Power vs. time

Figure 11 represents the graph which shows the VSWR of the output window shown below

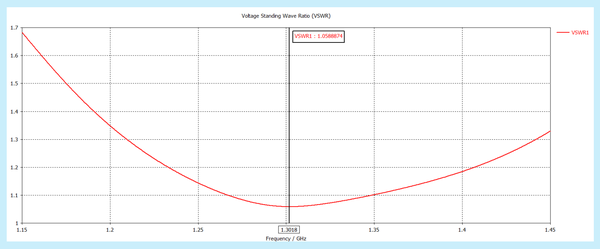

Figure 11: Voltage standing wave ratio

Conclusion and future Plan

I have successfully designed, simulated, and analyzed a key components (electron gun, magnet, RF structure and RF window) for a multi-beam klystron. The simulations, which used multiple software codes (AJDISK, KLYC, EMSYS, DGUN, POISSON and CST), showed close agreement, verifying their results.

The designed system achieved a high emission current and low perveance. A magnetic field of 1158 Gauss was used to focus the electron beam to a specific radius on the target. The very small (0.83%) current error between two of the software tools further confirmed the reliability of the design and the suitability of the software for this application.

Table 4: Emission Characteristics of the MBK

Parameters	Goal
Frequency	1.3GHz
Cathode Diameter	48mm
Current	130.8A
Electronic injection (Voltage)	115kV
Current density on Cathode	2.2A/cm²
Perveance	0.58 μP
Total Perveance	3.48 μP
Rrepetition rate	10Hz
pulse width	1.5ms
Electronic injections	6
Average Output Power	150kW
Cavities	6
Gain	48.5dB
Output efficiency	<80%
Beamlet current	21.8A
Cavity Mode	TM_{010}
Output Power	10.2MW
Magnetic field	1158Gauss

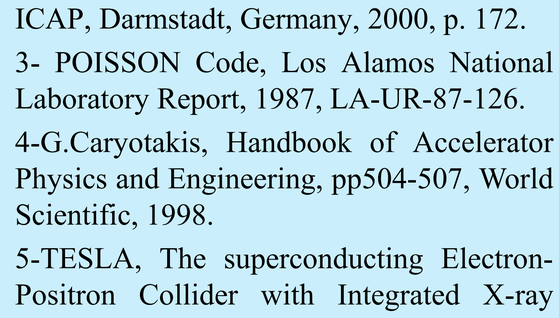

Figure 12:Integrated Design of the L-band 10MW MBK in CST

Figure 12 shows the Integrated Design of the L-band 10MW MBK in CST software.

To summarize the current status, the design has been basically completed, and the next step will begin soon.

References

1-A.Yano ,S.Miyake , THE TOSHIBA E3736MULTI-BEAM Proceedings of LINAC 2004, Lubeck, Germany.

2- A. Larionov, K. Ouglekov, DGUN-code for simulation of intensive axial-symmetric electron beams, in: Proceedings of 6th ICAP, Darmstadt, Germany, 2000, p. 172.

3- POISSON Code, Los Alamos National Laboratory Report, 1987, LA-UR-87-126.

4-G.Caryotakis, Handbook of Accelerator Physics and Engineering, pp504-507, World Scientific, 1998.

5-TESLA, The superconducting Electron-Positron Collider with Integrated X-ray Laser Laboratory, Technical Design Report.

6- User Manual, CST-Particle Studio, Darmstadt, Germany, 2020.

*** Work supported by Yifang Wang's Science Studio of the Thousand Talents Project**

The 2025 International Workshop on the High Energy Circular Electron Positron Collider (CEPC2025), Guangzhou, China, Nov 5-11, 2025

Development of High-Efficiency Energy-Recovery Klystrons*

Yu Liu[1,2], Zusheng Zhou[1,2†], Ouzheng Xiao[2], Fei Li[1], Yiao Wang[1,2], Han Xiao[1,2], Wenbing Gao[1,2], Fanyu Wang[1,2], Yunlong Chi[1,2]

1Institute of High Energy Physics, Chinese Academy of Sciences, Beijing 100049

2University of Chinese Academy of Sciences, Beijing 100049, China

中国科学院高能物理研究所 Institute of High Energy Physics Chinese Academy of Sciences

Based on the high efficiency klystron scheme of circular electron positron collider (CEPC), the depressed collector design is proposed to improve the overall efficiency of RF power source. The depressed collector technology has been applied in low power microwave electronic vacuum devices such as traveling-wave tube(TWT) and klystron for TV communications. The velocity of electrons entering the klystron collector is scattered, and it is difficult to use the depressed collector to sort the velocity of electrons. This paper presents a simulation study of the depressed collector for the high-efficiency klystron intended for the CEPC, establishes its basic design scheme, and demonstrates through simulation results that its efficiency can exceed 85%.

INTRODUCTION

The depressed collector is an important method to improve the efficiency of microwave tubes by recovering the energy of waste electrons. This technology has been widely used in TWT, and its collector recovery efficiency is more than 70%. Fig. 1 shows the basic principle of an energy recovery device. At present, the application of depressed collector on klystron is mainly used in low power klystron for TV and communication, but there is a little research on depressed collector technology of high power klystron. The fabrication and testing of the Phase I prototype have been successfully completed, marking the conclusion of the preliminary investigation into the energy recovery scheme. In Phase II, the energy recovery configuration specifically designed for the CEPC high-efficiency klystron will be experimentally validated. Simulation results have already demonstrated an efficiency exceeding 85%. Fabrication of the Phase II hardware is now underway, with high-power testing scheduled for August 2026.

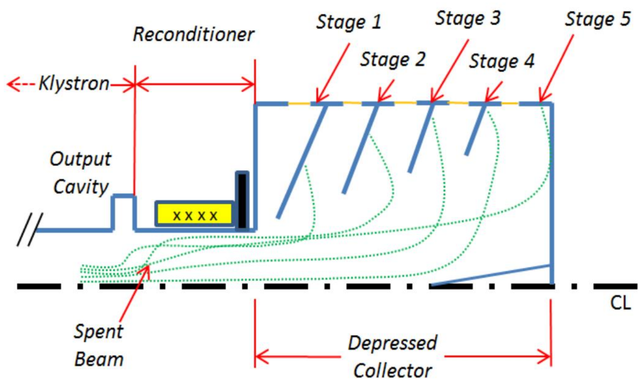

Fig.1.Depressed collector structure

DEPRESSED COLLECTOR PRINCIPLE

Based on the high efficiency klystron of CEPC, the depressed collector scheme is designed. The high efficiency tube has a saturated output power of 800kW and a design efficiency of more than 75%. The main design parameters of the high-efficiency klystron are shown in Table 1. High-power testing of the klystron was successfully completed in 2024(Fig 2).

Table 1: Klystron parameters of CEPC

Operating frequency	650 MHz
Output power	≥800 KW
Beam voltage	113 kV
Beam current	9.5 A
Beam perveance	0.25 μP
Efficiency	≥75%

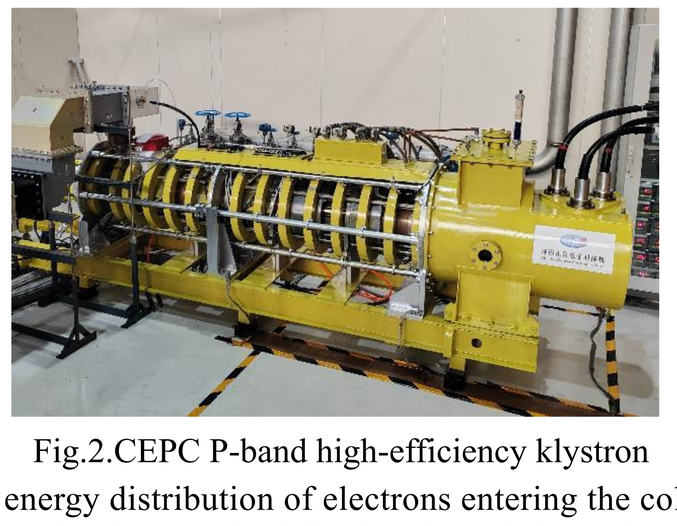

Fig.2.CEPC P-band high-efficiency klystron

The energy distribution of electrons entering the collector is shown in Fig. 2. The following formula is used to obtain the recovery power of the multi-stage depressed collector:

$$P_{rec} = \sum_{1}^{N-1} \int_{Vi}^{Vi+1} J_{waste}(V) I_0 V_i dV + \int_{V_N}^{\infty} J_{waste}(V) I_0 V_N dV$$

where Jwaste is the probability density function of electron energy distribution.

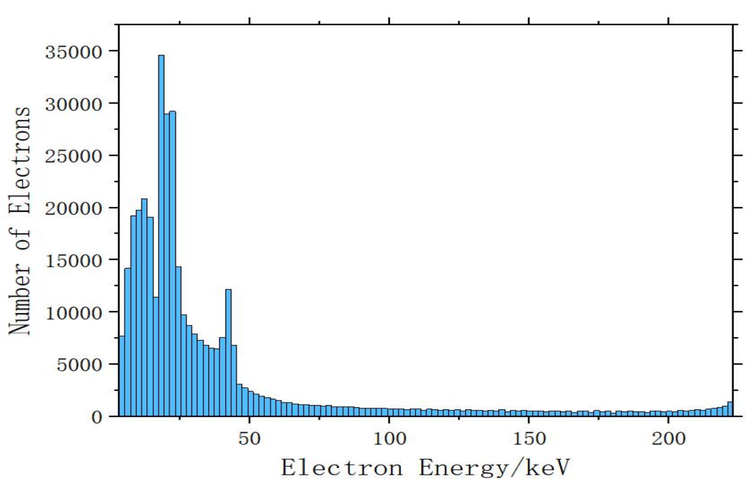

Fig.3.Energy distribution of waste electrons

VERIFICATION DEVICE

Before processing the depressed collector klystron, we use the energy recovery verification device to verify the key technology. The basic structure and machining of the verification device are shown in Fig. 4 and 5.

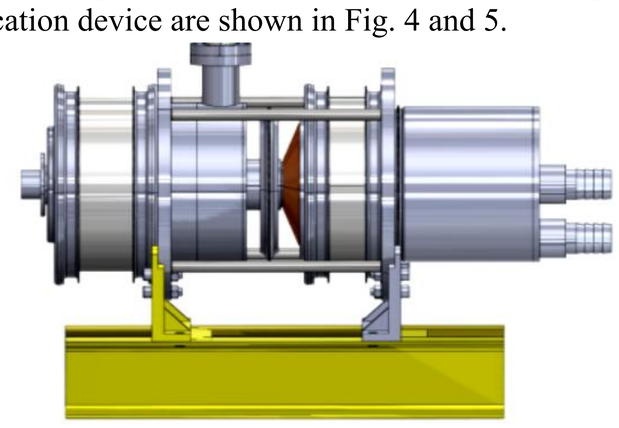

Fig. 4. Structure of energy recovery verification device

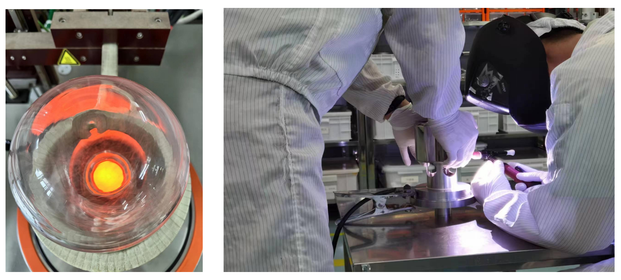

Fig. 5. Mechanical machining

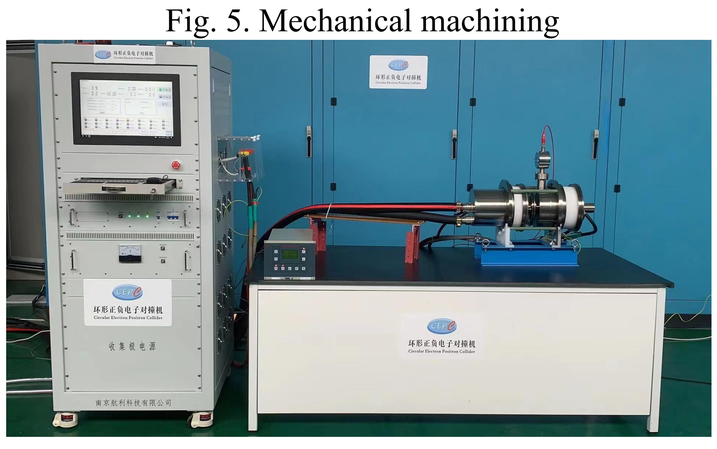

Fig. 6. Test platform

After the mechanical machining was completed, we proceeded with the setup of the test platform, as shown in Fig. 6. Testing was completed in November 2024, successfully validating the energy recovery technology(see fig7).

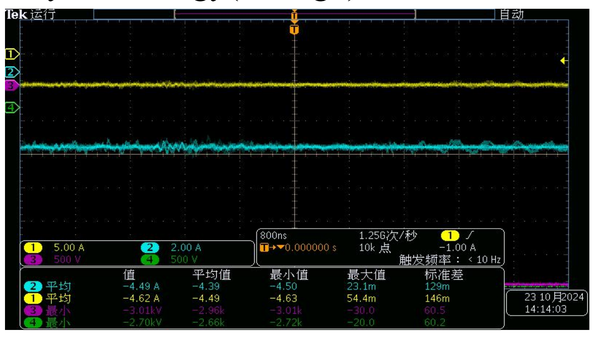

Fig. 7. Current and voltage waveforms

ENERGY-RECOVERY KLYSTRONS

In the second phase, we designed a single-stage depressed collector based on the prototype structure. The configuration is shown in Fig 8.

The electrode voltage is scanned in CST, and the results are shown in Fig. 9. Simulation results have already demonstrated an efficiency exceeding 85%. Fabrication of the Phase II hardware is now underway, with high-power testing scheduled for August 2026.

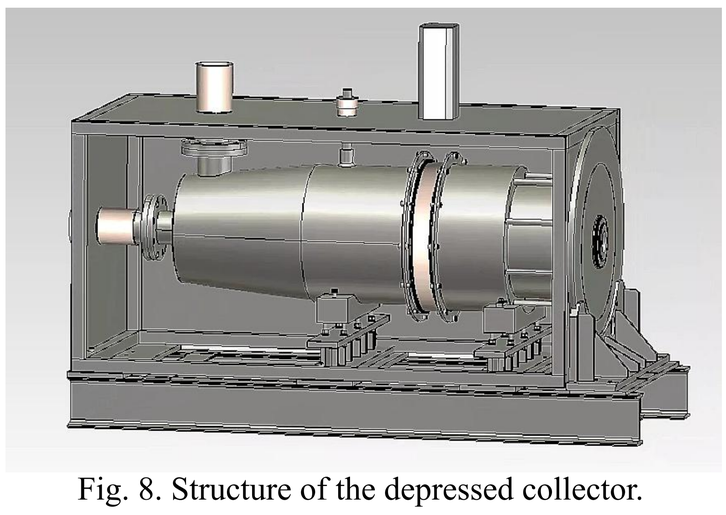

Fig. 8. Structure of the depressed collector.

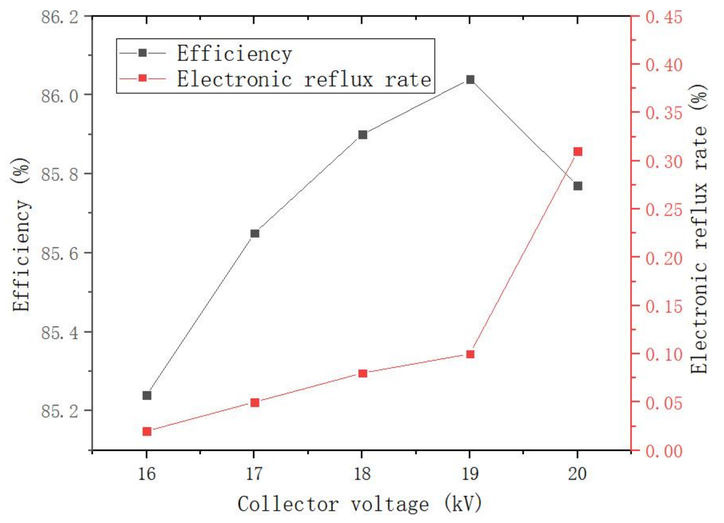

Fig. 9. Simulation results

SUMMARY AND OUTLOOK

This paper focuses on the high-efficiency CEPC klystron and conducts a theoretical analysis of the collector suppression, determining the electrode parameters. To validate the key technologies of the energy recovery klystron, an energy recovery verification device consisting of an electron gun and a collector was designed and fabricated. After completing the high-power testing, we will proceed with the design of a high-efficiency klystron with a depressed collector, aiming to increase the efficiency from 75% to over 85%.

REFERENCES

[1]Kosmahl H G. Modern multistage depressed collectors—A review[J]. Proceedings of the IEEE, 1982, 70(11): 1325-1334.

[2]DAYTON J A. System efficiency of a microwave power tube with a multistage depressed collector(Current distribution estimates for microwave power tube with depressed multistage collector)[J]. 1972.

[3]Jiang Y, Teryaev V E, Hirshfield J L. Partially grounded depressed beam collector[J]. IEEE Transactions on Electron Devices, 2015, 62(12): 4265-4270.

[4]Vaughan J R M. Synthesis of the Pierce gun[J]. IEEE Transactions on Electron Devices, 1981, 28(1): 37-41.

[5]Hamme F, Becker U, Hammes P. Simulation of secondary electron emission with CST PARTICLE STUDIOTM[C]//Proc. ICAP. 2006: 160-163.

* Work supported by Yifang Wang's Science Studio of the Thousand Talents Project

† email address: zhouzs@ihep.ac.cn

Research on an S-Band 50 MW High-Efficiency Permanent Magnet Klystron†

B04

Han Xiao[1,2], Zusheng Zhou[1,2]*, Ouzheng Xiao[1], Yu Liu[1,2], Yiao Wang[1,2], Wenbin Gao[1,2], Noman Habib[1,2], Fanyu Wang[1,2], Xiaobo Zhou[1,2], Yang Zhao[1,2],Munawar Iqbal[1], Abid Aleem[1]

[1]Institute of High Energy Physics, Chinese Academy of Sciences, Beijing 100049, China
[2]University of Chinese Academy of Sciences, Beijing 100049, China
*email address: zhouzs@ihep.ac.cn

中国科学院高能物理研究所 Institute of High Energy Physics Chinese Academy of Sciences

ABSTRACT

Improving klystron efficiency is crucial for reducing the operational costs of particle accelerators. This study presents an S-band 50 MW periodic permanent magnet (PPM) focusing high-efficiency klystron , aiming to minimize energy consumption while maintaining high conversion efficiency. The research addresses the domestic need for localized development of S-band 50 MW klystrons. A key focus is the design of a high-efficiency 50 MW klystron and its corresponding PPM focusing structure. Through precise computer simulations of beam dynamics, the feasibility of the PPM focusing system is validated, achieving both high microwave conversion efficiency and compatible beam focusing. The development of this S-band PPM klystron represents a significant advancement in klystron technology, offering a more efficient and cost-effective solution for high-power applications. This design reduces power consumption without compromising performance, contributing to the broader goals of energy efficiency and cost reduction in accelerator technology.

INTRODUCTION

High power and high efficiency are key research priorities in klystron development. The advancement of large-scale scientific projects—such as the International Linear Collider (ILC), Compact Linear Collider (CLIC), Future Circular Collider (FCC), and Circular Electron Positron Collider (CEPC)—highlights the essential role of high-efficiency klystrons in these initiatives. Improving klystron efficiency relies on effective bunching of peripheral electrons and reduction of velocity dispersion. Common strategies to this end include lowering electrical conductivity and incorporating second harmonic cavities.

Permanent magnet focusing eliminates the need for conventional focusing coils, along with their dedicated power supplies and cooling systems. This not only reduces power consumption but also substantially cuts the klystron's size and weight.

This study introduces a design that integrates high efficiency with permanent magnet focusing, aiming to enhance klystron performance while facilitating system miniaturization.

PERIODIC PERMANENT MAGNET FOCUSING

The Periodic Permanent Magnet (PPM) focusing system is comprised of rings of axially magnetized permanent magnets arranged with alternating polarity. An electron beam can remain focused within this resulting periodic magnetic field, yet its envelope exhibits fluctuation. The amplitude of this fluctuation increases as the beam voltage decreases. Beyond a well-defined threshold, the beam becomes completely divergent. A key advantage of this configuration is its enhanced utilization of the reverse magnetic fields between adjacent magnets, leading to a more compact and lightweight focusing system.

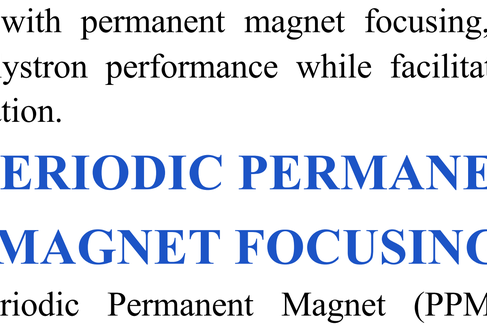

Figure 1 Periodic permanent magnet focusing structure

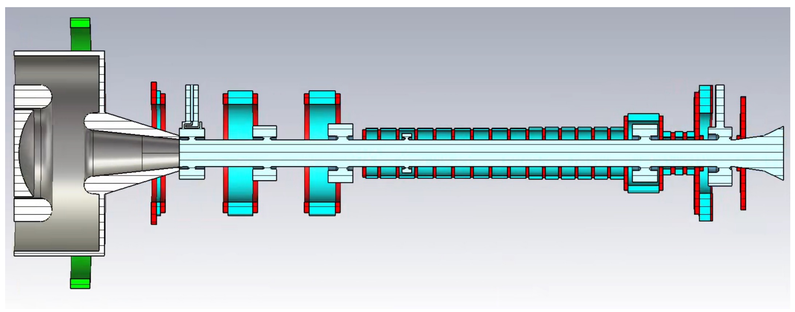

Figure 2 Focusing structure and vacuum inside the klystron

FOUNDATION DESIGN

The design incorporates six cavities, one of which is a second harmonic cavity. Its focusing structure is mainly divided into three sections. The first section has a small fundamental current of the beam and is designed as a long-period magnetic field that is easy to process. At the same time, considering the water cooling space, a large inner diameter magnetic ring is used. In the second section, the pole shoe extends into the vacuum inside the klystron, and considering the cavity size, it is designed as a medium-period medium inner diameter structure. The third section has a large fundamental current and is designed as a short-period small inner diamete structure.

Table 1 Main parameters of klystron

Frequency	2856Mhz
Output power	50MW
Voltage	350kV
Current	272A
Beam radius	9mm
Drift tube radius	13.8mm
Efficiency	53%

ELECTRON OPTICS

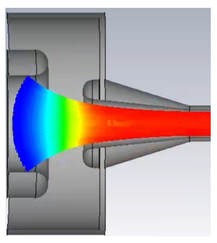

Figure 3 The electron gun in CST

In CST simulation, the electron gun current is 272A, the waist radius is 8.86mm, the minimum period length of the focusing structure is 24mm, and the maximum magnetic field along the axis is 1614Gs.

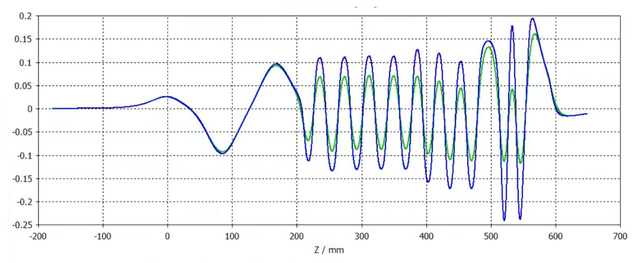

Figure 4 Magnetic field distribution at the axis and beam radius

BEAM DYNAMIC

The beam dynamics design was first completed in AJDISK and then rigorously verified and optimized through simulations in CST. The PIC simulations confirm a stable output of 51.2 MW with an efficiency of 53.8%.

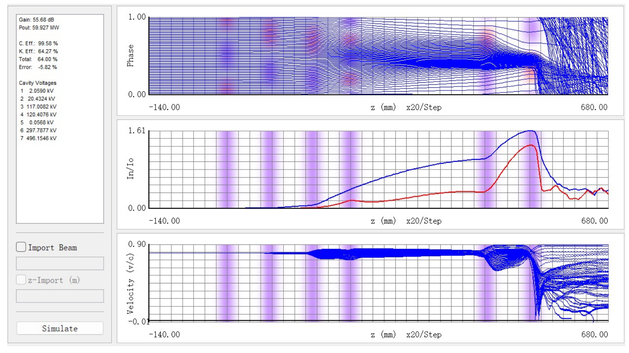

Figure 5 Simulation results in AJDISK

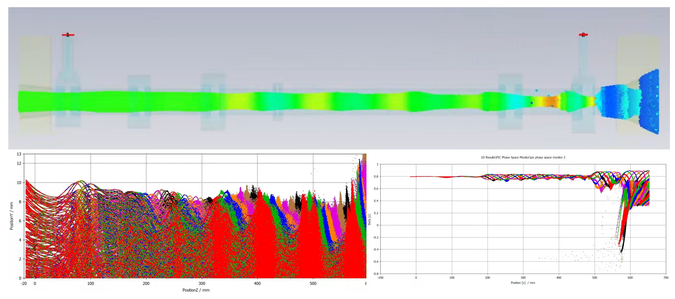

Figure 6 Beam trajectory and phase space in CST

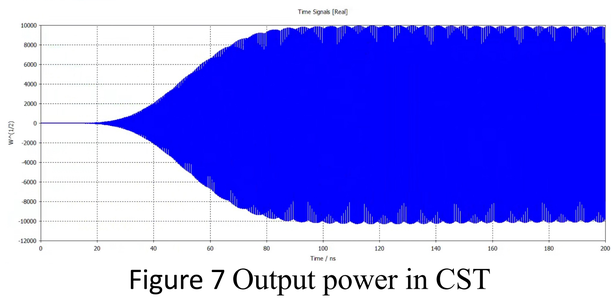

Figure 7 Output power in CST

SUMMARY AND OUTLOOK

This study proposes a design of an S-band 50MW high-efficiency permanent magnet klystron, characterized by a second harmonic cavity and segmented periodic permanent magnet focusing. This configuration has the advantages of high efficiency, simplicity, and compactness. The CST simulation results show that the output power is 51.2MW and the efficiency is 53.8%.

The next step is to optimize the reflux electrons and output power.

REFERENCES

[1] Syratchev, I. (2022). High efficiency klystrons. [PowerPoint slides]. https://indico.cern.ch/event/1138690/contributions/4782684/attachments/2435633/4171251/IFAST_2022_SI.pdf

[2] Matsumoto, H., Shintake, T., Ohkubo, Y., Taoka, H., Ohhashi, K., & Kakuno, K. (2001). High power test of the first C-band (5712 MHz) 50 MW PPM klystron. PACS2001. Proceedings of the 2001 Particle Accelerator Conference (Cat. No.01CH37268), 2, 993-995 vol.2.

[3] Chin, Y.H., Matsumoto, S., Mizuno, H., Morozumi, Y., Ohkawa, T., Ohya, K., Takata, K., Toge, N., Tokumoto, S., Kazakov, S.Y., Larionov, A., & Teryaev, V.E. (2001). X-band PPM klystron development for JLC. PACS2001. Proceedings of the 2001 Particle Accelerator Conference (Cat. No.01CH37268), 5, 3792-3794 vol.5.

[4] Sprehn, D.W., Caryotakis, G., Jongewaard, E.N., & Phillips, R.M. (1999). Periodic permanent magnet development for linear collider X-band klystrons.

[5]CST GmbH, Darmstadt, Germany.

†Work supported by Dr. Yifang Wang's Science Studio of the Thousand Talents Project

The 2025 International Workshop on the High Energy Circular Electron Positron Collider (CEPC2025), 5-10 November, Guangzhou, China

B05

Heat Load Investigation of Collector for High-Average Power Beam Dump of 80 MW Klystron for CEPC LINAC

Munawar Iqbal, Z. S. Zhou*, O. Z. Xiao, N. Habib, A. Aleem, Y. Liu, Y. A. Wang, and H, Xiao

Institute of High Energy Physics, Chinese Academy of Sciences, Beijing100049, China

*Corresponding Author email: zhouzs@ihep.ac.cn

Abstract: *For the average output power of the C-band klystron for CEPC LINAC, the power capacity and stability of the collector are investigated.. We terminated the magnetic field at the collector entrance to defocus the beam for a higher beam spread for lower heat load without using any extra reverse coil. The klystron, driven by a 425-kV, –416-A electron beam, can withstand a maximum beam power of 177 MW at zero RF drive. Thermal results indicate, with 0.03% duty factor an average power of 52 kW in the collector, a maximum temperature < 88 ºC is measured on the collector with an optimized cooling system. The simulated and theoretical temperatures are in agreement. The power capacity, cooling efficiency, and stability analysis of the collector are carried out in this article. The results establish the high-power capacity and integrity of the collector.*

Introduction

The power of the unspent beam depends on the *RF efficiency, beam tunnel, and field* profile of the magnet primarily applied to the electron beam focusing for its transportation downstream. Lower klystron efficiency leads to high power of the unspent beam in the collector. Typically, with higher frequency the electron beam tunnel gets smaller, that finally increases the thermal load on the collector due to smaller beam radius of the spent beam. The magnetic field after the cavity region reduces (adiabatic decompression) toward the collector region. Since the electron trajectories follow the magnetic field lines, therefore the transverse momentum of the electron beam decreases, and finally, the electron beam is collected at the collector surface. The dissipated energy generates heat energy which may rise the temperature to the melting point of the collector.
In case of the non-adiabatic decompression method, the longitudinal momentum of the electron is converted into the transverse motion increasing the Larmor radius. The electron beam has to spread over a large area to reduce the heating effects on the collector surface. We conducted thermal analysis on the collector, using CST TRK [1] to obtain the particle trajectory of the electrons entering the collector and converting it into heat flux density, serving as the heat source for the thermal analysis. CST THS is used to analyze the thermal characteristics of the collector electrode and optimize to achieve relatively an ideal temperature for the collector.

Design & Description

For CEPC LINAC klystron, a 177 MW power DC electron gun operating at 425-kV accelerating potential with space charge current 416-A serves as the power source to obtain 80 MW RF output power with 47 % efficiency. At 80 MW RF output power with 0.03% duty cycle (100 Hz & 3 µs), the average beam power is 24-kW. However, at full DC beam power (177 MW) without RF drive (unmodulated beam), the average beam power is scaled to be 52-kW at the same duty factor. This high power has to be dissipated inside the collector surface and need to be dumped for an efficient operation of the klystron. The power features of 80 MW C-band klystron are given in Tab le 1. The specifications of the coils are given in Table 2.

Table 1: Klystron's DC & RF power features

Parameter	Value	Unit
Gun current	416	A
Gun voltage	425 kV	kV
DC beam Power	177	MW
RF output Power	80	MW
Duty cycle	$3*10^{-4}$	-
Average output power w/o RF drive	52	kW
Average output power with RF drive	24.	kW

Table 2: Magnets' coils Specifications

Coils #	Reference/Conceptual Magnet Coils Current density (A/mm^2)	Optimized/Engineering Magnet Coils Current density (A/mm^2)
Reverse Coil	1.17	0.866
1st	5.955	2.675
2nd	1.899	2.675
3rd	2.776	1.205
4th	2.726	0.873
5th	3.540	0.996
6th	-	1.518
7th	-	1.456
8th	-	2.453
9th	-	2.346

1. Magnets' Design, Description & Simulation

The electromagnet is designed with the main goal to have field profile that minimize the magnetic field transverse components for the smallest beam ripples all over beam until the start of the collector. It also must provide a field configuration in the collector region to reasonably minimize the heat load on the collector surface. Firstly, we design a baseline magnet (conceptual design) in CST and obtained a reference field for the static and dynamic beam simulations, and successfully got the required DC & RF parameters of the klystron and then optimized this field by keeping the profile same by changing the design of the magnet (engineering design) for lower heat loads at the coils and also on the collector to avoid any thermal runout. The two magnets' designs are shown in Figure 1 (a,b), where the iron regions (pole pieces) are similar however, the coils are different in numbers and cross-sections. The design of the magnets are different but the profiles are similar except on the collector region as evident from the Figure 2a, the optimized field is terminated at 691.5 mm but the reference filed is still effective until 952 mm. Similarly, the radial component of the field in the optimized magnet has lower value 1.31 Gs compare to the reference magnet radial component 3.31 Gs as shown in the Figure 2b. The optimized magnet has lower coils current densities which requires no extra cooling system as the Ohmic losses in power consumption of a coil drop linearly with reduction in the current density [2].

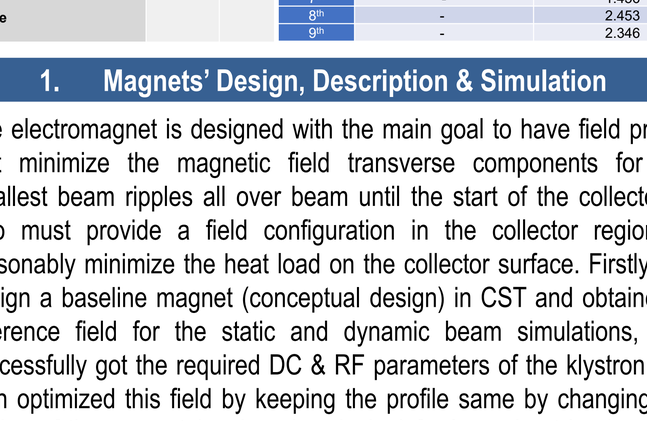

Figure 1: a) Reference and, b) optimized design of the Magnets

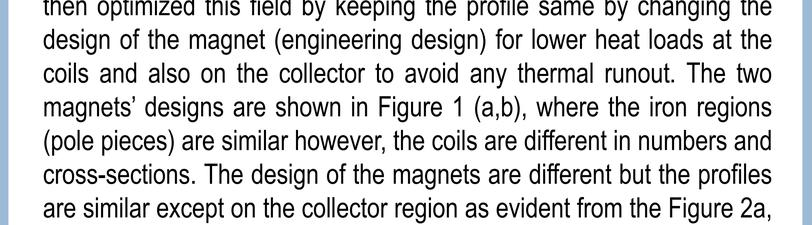

Figure 2: Magnets' field profiles and comparison a) axial and, b) radial fields

2. Collector Design and Description

Heat load by the beam impingement on the collector surface and then the heat removal from the collector surfaces are two different scenarios for thermal analysis of the collector. Heat removal is a mature & established phenomenon and is a function of heat exchangers' geometry, material types & thickness, and heat transfer coefficient (type & velocity of the fluid) of the collector. Heat load is greatly dependent on the power of the incident beam P, and surface area of the collector. The dissipated power density at the collector wall, H is [3]:

$$H = \left[\frac{r_i}{r_a}\right]^2 \times 174 \frac{r_i}{b} P^{0.5} \left[ln\frac{r_a}{r_i}\right]^{0.5} D_o$$

r_i = radius of the individual beam trajectory, b = radius of the beam before spread, r_a = radius of the collector, P = beam perveance, and, $D_o = {I_o V_o}/{\pi b^2}$, ($I_o V_o$ are current & voltage of the beam). The power of the incident beam greatly depends on the position of the beam launching into the collector which is a function of the RF output power (efficiency of the klystron) and the filed profile of the magnet. We used the full DC beam without RF drive; hence the klystron efficiency is ruled-out in this analysis. Oxygen free high conductivity copper (OFHC), collector with high-power capacity and stability has been designed in CST as shown Figure 3 (a,b,c), in accordance with the fully-established SLAC 5045 design [4] using similar dimension and grooving geometry due to its similar average output power 45 kW with modulated beam. It has a double walled water jacket for heat protection.

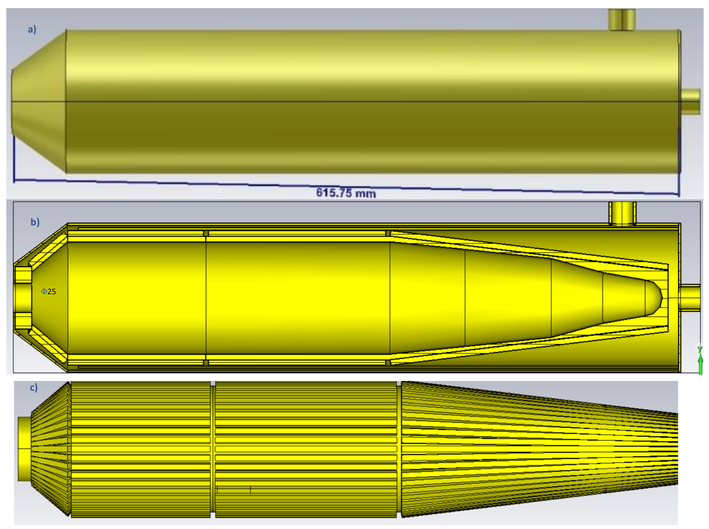

Figure 3: a) outer view of the collector, b) cut view showing double water jacket, c) grooves on the collector

Results and Discussions

A full power DC beam @ 425 kV & 416 A without RF drive (unmodulated beam) is launched from the cathode under the influence of the filed profiles of the magnets shown above. A 177 MW power beam hits the surface of the collector as shown in the Figure 4.

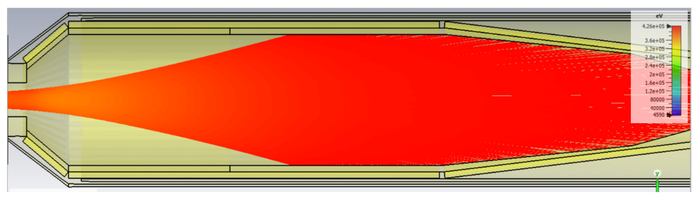

Figure 4: Cut view of electron beam profile in the collector @177 MW DC beam power

The beam has same characteristics under the two profiles as the profiles are similar at the beam optics and RF regions except different at the collector region. The beam envelope in red is hitting the surface at 870 mm while the blue one is hitting the surface earlier than the red at 834 mm, respectively. This is due to the effect of the magnetic field penetration into the collector. In case of reference field profile; a 529 Gs field (Fig. 5a) is still entering the collector and keep the beam still focus and hence more powerful to hit at the collector surface at 870 mm. While under the optimized field, this filed is 0 Gs at the entrance of the collector as shown in in Figure 6a, hence beam quickly diverges and hit the collector surface earlier at 834 mm and will have lower power density comparatively

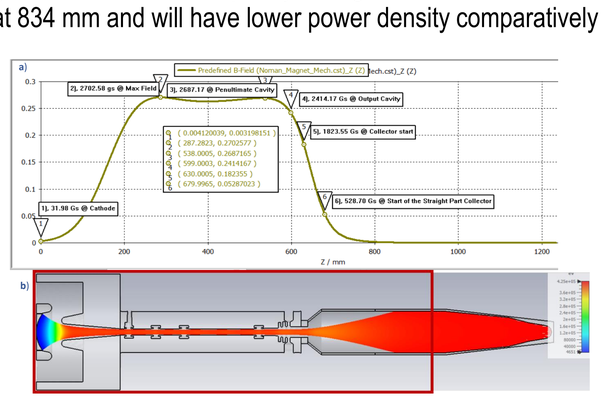

Figure 5: a) Reference magnetic field profile, b) Beam trajectories from the cathode, RF section and then in the collector

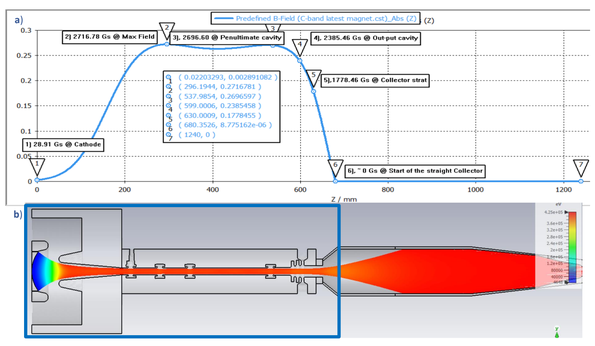

Figure 6: a) optimized magnetic field profile, b) Beam trajectories from the cathode, RF section and then in the collector

The red and blue boxes in the Figures 5b & 6b show the effectiveness of the magnetic fields in both scenarios. This effectiveness is lower in the optimized filed and is finished at the tapered part of the collector. Moreover, it determines the temperature rise on the collector surfaces. The beam hit the inner surface of the collector and transfer its heat to the surface and consequently rises the temperature of the collector surface. The full beam power, 177 MW is scaled to more than 52.0 kW average power due to the duty factor of 03 µs and 100 Hz of the RF signal. Under the influence of reference filed, we noted maximum temperature 329 ºC on the inner surface of a flat collector (not shown here). This maximum temperature is reduced to 162 ºC by incorporating the grooves on the outer surface of the collector as shown in Figure 7.

However, by using optimized filed profile, the maximum temperature reduces to < 88 ºC. These temperature and profiles are shown in the Figure 8. With an input heating power, P = 52 kW and surface area of the cylinder, A = 175000 mm^2, for a convective heat transfer coefficient, h = 5000 W/K.m^2, the change in temperature is given by the Newton's law of cooling [5]:

$$\Delta T = \frac{P}{h.A} = 59.43\ ^oC$$

The temperature rise is; 59.43 ºC + 25 ºC = 84.43 ºC with 25 ºC ambient temperature. There is a < 4.0 % difference between the theoretical and simulated values (87.75 ºC). The maximum temperature is well below the required limit. Higher cooling coefficient corresponds to the higher flow rate which has more turbulence for efficient heat removal.

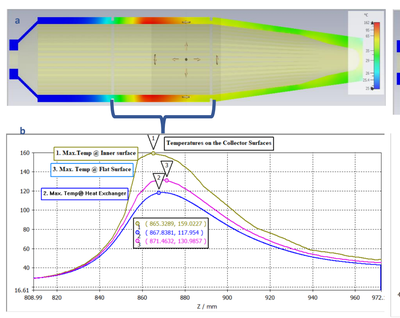

Figure 7: a) Cut view of temperature dissipation at the inner collector surfaces with Ref. field and, b) corresponding temperature profiles at the surfaces (inner, flat & heat exchanger)

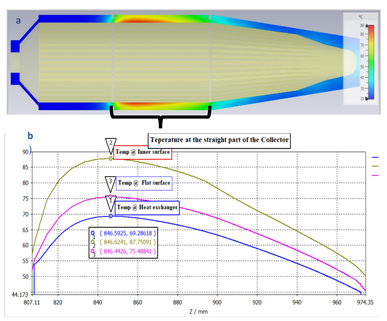

Figure 8: a) Cut view of the temperature dissipation at the collector surfaces with optimized field, and b) the corresponding temperature profiles at different surfaces.

We also compared the power level and temperature rise of the different klystrons' collectors. Moreover, the SLAC 5045 klystron collector was designed in CST to compare the temperature as given in Table 3. The C-Band CEPC collector temperature is found lower and hence confirms the thermal stability and integrity of the collector.

Table 3: Comparison of Max. Temp. at different klystron Collectors' surfaces.

Sr. #	Article Name	Power Dissipated	Max. Temp
1	S-Band klystron collector	14 kW CW	395 ºC [6]
2	Q-Band Gyro-TWT collector	50 kW Avg. Power	381 ºC [7]
3	W-band Gyro-TWT collector	96 kW Avg. Power	194 ºC [8]
4	C-Band Klystron Collector	250 kW CW	73.15 ºC [9]
5	5045 SLAC SBAND Collector	45 (90.72 w/o RF) kW Avg. Power	104 ºC [4]
6	80MW CBAND CEPC Collector	24 (52 w/o RF) kW Avg. Power	87.75 ºC [this paper]

Conclusion

We successfully terminated the field entering into the collector to obtain a lower thermal load with the same magnetic design used for the static and dynamic beam analysis without using any extra reverse coil on the collector region. It can be seen from the result that the highest temperature of the collector is 87.75 ºC, the melting point of the oxygen-free copper is 1083 ºC, far higher than the highest temperature. The collector will handle both the unmodulated beam (the beam that passes through all the cavities with no RF power applied), and the modulated beam (when the beam is subjected to the input RF power in the input cavity and excites and interacts with RF fields in all other cavities). In the case of the unmodulated beam, the developed collector will dissipate the entire beam power of 177 MW very efficiently. In other case, (modulated beam), the collector will dissipate less power around 94 MW, which corresponds to a tube efficiency of 47%. After the engineering design, the Magnet & the collector is now under fabrication alongside the gun and RF cavities.

References

1. User Manual, CST-Particle Studio, Darmstadt, Germany, 2020.
2. Shchelkunov, Sergey, Hirshfield, Jay L, Jiang, Yong, *50kW CW Multi-Beam Klystron, Technical Report*, Omega-P R&D., Inc. 07 January 2019.
3. Udaybir Singh & A. K. Sinha, Electron Gun for Gyrotrons, Springer Briefs in Applied Sciences and Technology, Springer Singapore, 22 August (2022).
4. Aaron Jensen at al., 25-year performance review of the SLAC 5045 S-band klystron, SLAC PUB-16045, 2nd Int. Particle Accelerator Conference Spain, (IPAC 2011), September 4 - 9, (2011).
5. Theodore L. Bergman, David P. DeWitt, Frank P. Incropera and Adrienne S. Lavine, Introduction to Heat Transfer", Hoboken, NJ: John Wiley & Sons, Inc., June 7, 2011.
6. A. V. Konnov, et al., Thermal analysis of multibeam klystron collector with forced air cooling, 10th Int. Vacuum Electron Sources Conference (IVESC), St. Petersburg, Russia, 2014.
7. Wei Jiang, Chaoxuan Lu, Binyang Han, Guo Liu, Jianxun Wang, Youlei Pu, and Yong Luo, Experiment and Power Capacity Investigation of Collector in the 50-kW-Average Power Q-Band Gyro-TWT, *IEEE Transactions on Electron Devices*, **70** (8) (2023), 4372- 4378.
8. Wei Jiang et al., Curved Geometry Collector Design for High Power Gyro-TWT, Vol. 65, No. 6, (2018)
9. Suman Baloda et al., Design and development of collector for C-band 250 kW CW Klystron, *Journal of Physics: Conference Series* 390 (2012) 012076.

B06

Development of S-band high efficiency klystron

Y. A. Wang[1,2], Z. S. Zhou[1,2], O. Z. Xiao[1], Y. Liu[1,2], H. Xiao[1,2], F. Li[1], W. B. Gao[1,2], M. Iqbal[1], A. Aleem[1], F. Y. Wang[1,2], Y. L. Chi[1], Noman Habib[1,2]

[1]Institute of High Energy Physics, Chinese Academy of Sciences, Beijing 100049, China
[2]University of Chinese Academy of Sciences, Beijing 100049, China

中国科学院高能物理研究所
Institute of High Energy Physics
Chinese Academy of Sciences

Abstract

To address the evolving technical demands of particle accelerator technology and the radio frequency (RF) power supply specifications for the Linear Accelerator of the Circular Electron Positron Collider (CEPC), this study develops an S-band short-pulse klystron. By adopting the high-efficiency Bunching Alignment and Collecting (BAC) method, the klystron achieves an efficiency of 55% and a peak power of 80 MW, which enables high-power output while reducing energy consumption and provides a practical technical solution for accelerator RF sources. Currently, the klystron is in the mechanical processing stage, and subsequent high-power tests will be conducted to verify its operational performance.

Background

The development of large particle accelerators necessitates klystrons capable of providing megawatt-level power, which results in high energy consumption and operational costs. Therefore, enhancing the efficiency of klystrons can enable higher RF power generation while simultaneously reducing energy consumption and operating costs, thereby promoting environmentally friendly and sustainable solutions.

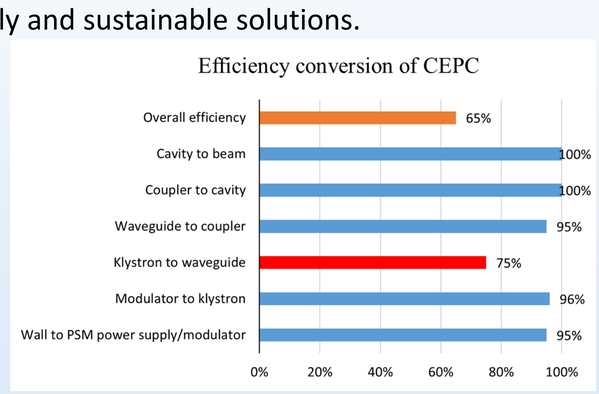

Figure 1 Overall efficiency of CEPC power sources

Design of electronic optical system

The required parameters for the electron gun in this design are a voltage of 350 kV, a current of 415 A, and a beam radius of 8.65 mm. Through computational optimization, the electron gun is verified in CST to achieve a current of 415 A, a maximum beam radius of 8.67 mm, and a beam fluctuation rate of 5.1%.

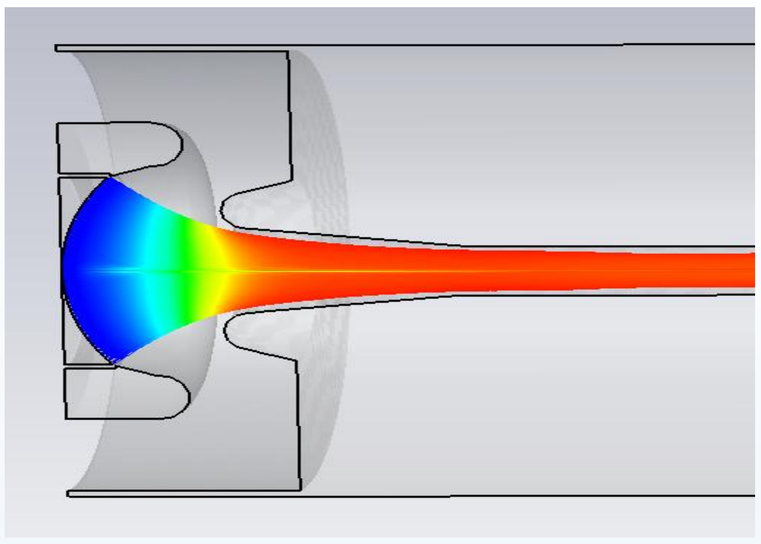

Figure 2 The electron gun in DGUN

The coil structure and magnetic field distribution are verified in CST.

The focusing magnetic field used in the electron gun is provided by the coil structure

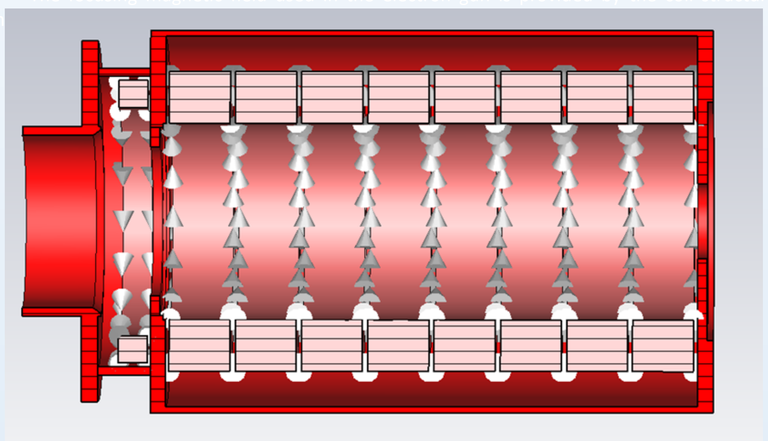

Figure 3 The coil structure in CST

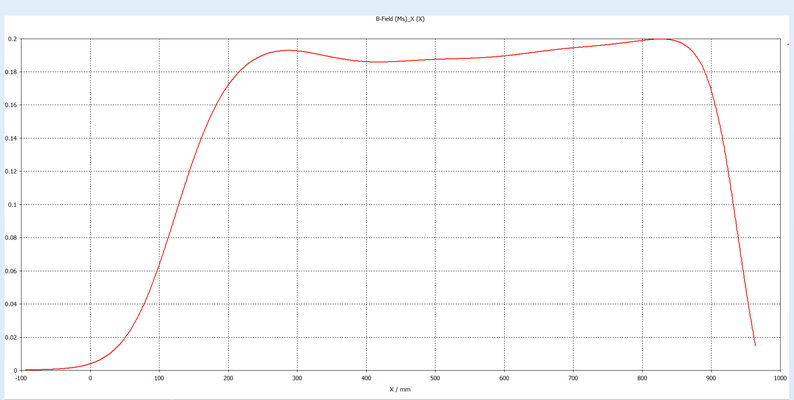

Figure 4 Magnetic field distribution in CST

Beam dynamic

Using 8 resonant cavities, the fifth resonant cavity is a second harmonic cavity. In 3-D CST, the RF conversion efficiency of the klystron was determined to be 55%, with an output power of 80 MW.

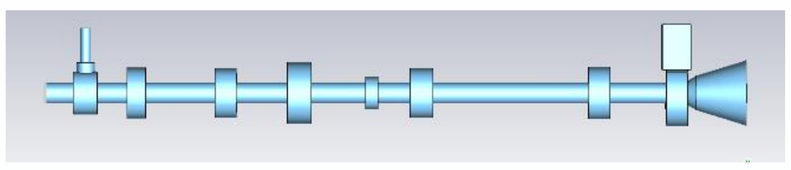

Figure 5 Structure of the klystron

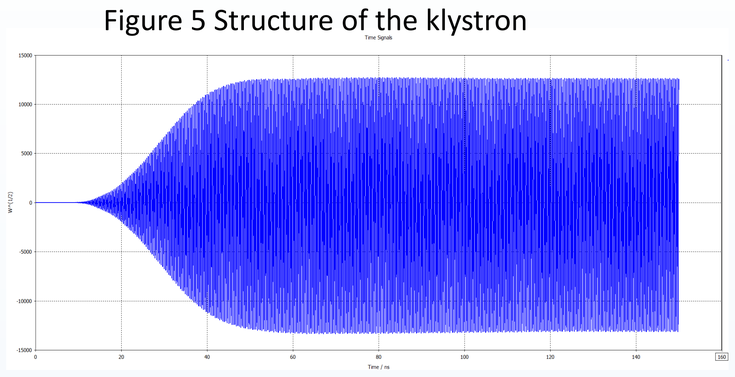

Figure 6 The power output in CST

In simulations across different dimensions, the output efficiency of the klystron is simulated by varying its input power, resulting in the acquisition of the klystron's transfer characteristic curve. The relationship between the input power and output efficiency of the klystron is illustrated in Figure 7.

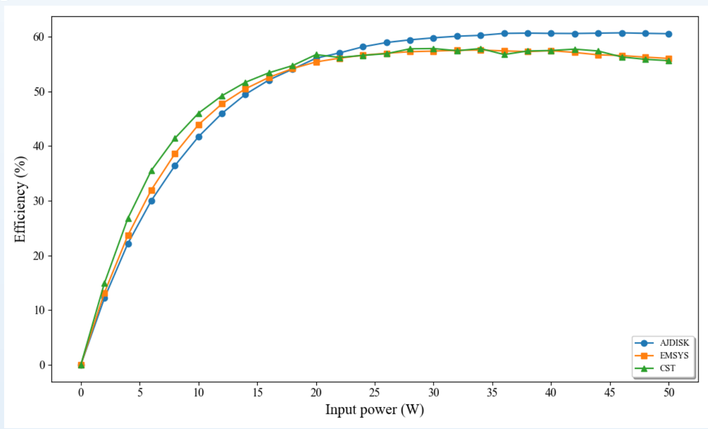

Figure 7 Klystron transfer curve

In the 2-D simulation, with the excitation fixed at 30W, the 1dB bandwidth of the klystron is found to be 22MHz by scanning the frequency. The gain curve is shown in Figure 8.

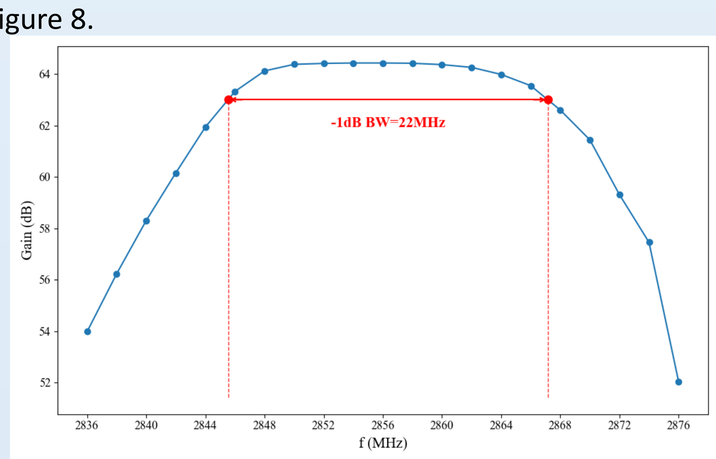

Figure 8 The gain and excitation signal frequency

Cavity machining and testing

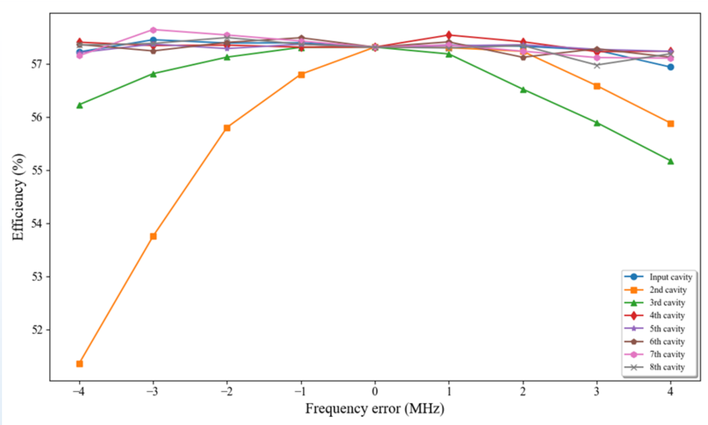

Figure 9 frequency and efficiency of the cavities

At present, the mechanical design and part processing have been completed. To control the machining tolerance, an error analysis of the cavity frequency is conducted, and the influence of the frequency variation of each cavity on the efficiency is illustrated in Figure 9.

The testing of the intermediate cavity is shown in Figure 10. Subsequently, the design values are compared with the test values, as presented in Table 1. The actual cavity test meets the design requirements.

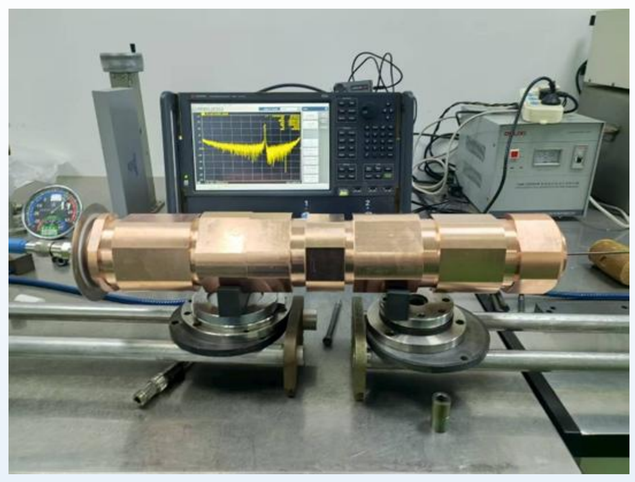

Figure10 The intermediate cavity assembly structure

Table 1 Design Values and Test Values of Cavity Frequency

Cavity	Design value(MHz)	Measure value(MHz)
1	2859	2857
2	2853	2853
3	2870	2871
4	2326	2328
5	5558	5559
6	3010	3010
7	3065	3065
8	2852	2853

Conclusion

Based on Pierce electron gun theory, this study modeled and optimized the electron gun in the electron optical system, with all parameters meeting design requirements.

Using the BAC method for beam dynamics design, 3D simulation verified a final output power of 80MW and an efficiency of 55%.

Calculations obtained the transfer characteristic curve, which shows klystron efficiency rises with excitation power and finally stabilizes. The 1dB bandwidth was calculated as 22MHz, meeting design requirements.

Currently, mechanical design, component processing, and cavity cold testing are complete, with the cavity frequency meeting design specs. Future work will focus on high-power testing.

References

[1] R.V. Egorov,I.A.Guzilov,“BAC-klystron: a new generation of klystrons in vacuum electronics” , Moscow University Physics Bulletin, Vol. 74, No.1, pp 38-42,2019.

[2] Gao, Jie . "CEPC Technical Design Report: Accelerator." Radiation Detection Technology and Methods 8.1(2024):1-1105.

[3] Guzilov, I. A. . "BAC method of increasing the efficiency in klystrons." Vacuum Electron Sources Conference IEEE, 2014.

[4] CST GmbH, Darmstadt, Germany.

[5] Guzilov, Igor , et al. "Comparison of 6 MW S-band pulsed BAC MBK with the existing SBKs." (2017).

[6]S. G. Tantawi, et al. "Beam-wave interaction studies for the development of high-efficiency klystrons." IEEE Transactions on Electron Devices 60.6 (2013): 2014-2022.

* Work supported by Dr. Yifang Wang’s Science Studio of the Thousand Talents Project

† email address: zhouzs@ihep.ac.cn wangya@ihep.ac.cn

Poster ID :27

B07

The 2025 International Workshop on the High Energy Circular Electron Positron Collider (CEPC2025), GuangZhou, China, Nov 5-10, 2025

Development of 1.2 Mega-Watt P-band Travelling Wave Resonant Ring*

Fanyu Wang[1,2], Zusheng Zhou†[1,2], Ouzheng Xiao[1], Yiao Wang[1,2], Yu Liu[1,2], Wenbing Gao[1,2], Han Xiao[1,2], Fei Li[1], Nan Gan[1], Noman Habib[1,2], Munawar Iqbal[1], Abid Aleem[1]

[1]Institute of High Energy Physics, Chinese Academy of Sciences, Beijing 100049, China

[2]University of Chinese Academy of Sciences, Beijing 100049, China

中国科学院高能物理研究所 Institute of High Energy Physics Chinese Academy of Sciences

ABSTRACT

To ensure the safety and reliability of high-power microwave devices like ceramic windows and couplers in accelerators, the Institute of High Energy Physics (IHEP) is developing a P-band Traveling Wave Resonant Ring (TWRR) for efficient high-power testing to support the development of klystrons in CEPC[1]. This system, comprising a main directional coupler, a power detection coupler, 4 H-bends, an observation window, a 3-stub tuner, and a phase shifter, is designed to test ceramic window at 1.2 MW (1.5 times the rated power of an 800-kW klystron) to significantly reduce the risk of window breakdown.

INTRODUCTION

A resonant ring, also known as a traveling wave resonat Ring(TWRR), is a loop of waveguide which can amplify apparent power through the coupling of waves at its input. Figure 1 shows a basic resonant ring circuit.

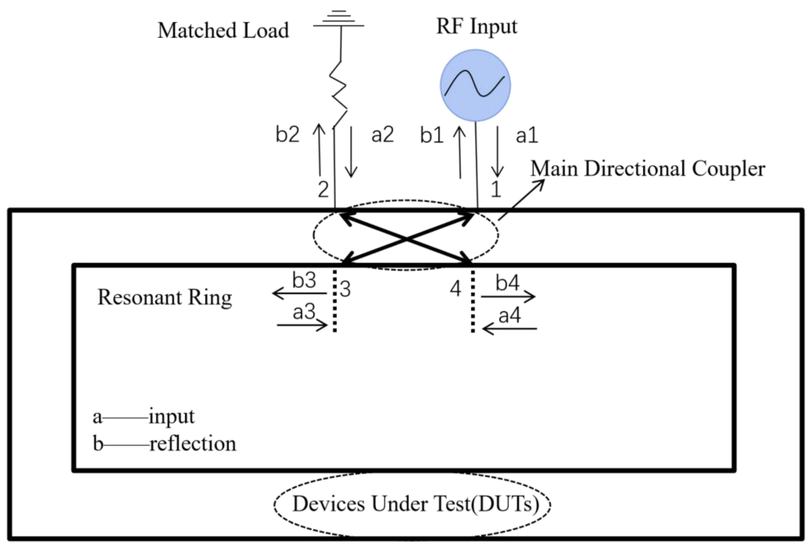

Figure 1 Basic Resonant Ring Circuit

PRINCIPLE

Power superposition process is showed in figure 2. Power is initially input to port 1 and then coupled into the ring through port 3. Uncoupled waves continue through port 2, which is typically terminated by a load, while the waves within the ring travel through ports 3 and 4. With the appropriate ring length and matching,these waves add constructively, resulting in a voltage increase that functions as power gain within the ring.

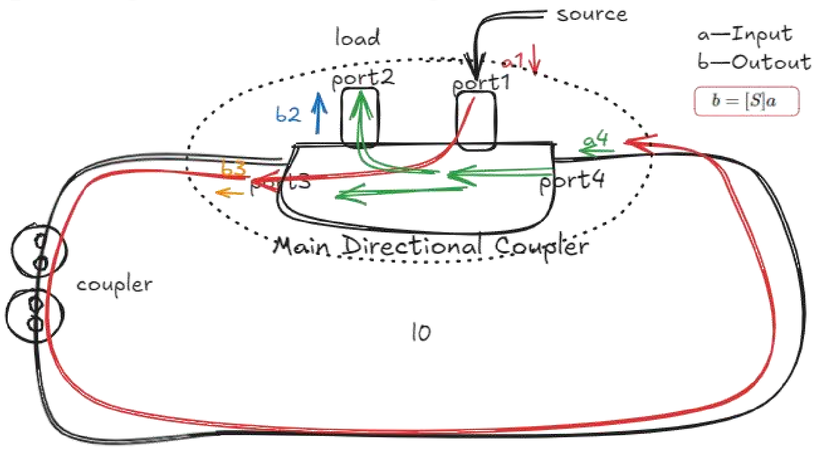

Figure 2 Power Superposition Process

POWER GAIN

$$M=\frac{C^2\left(1-e^{-\alpha L}\sqrt{1-C^2}\sqrt{1-r^2}\right)^2}{\left(1-2e^{-\alpha L}\sqrt{1-r^2}\sqrt{1-C^2}+e^{-2\alpha L}(1-C^2)\right)^2}$$

Where C is the coupling coefficient of the directional coupler, r is the reflection coefficient in the ring, $e^{-\alpha L}$ is the attenuation in the circuit, α is the effective attenuation coefficient, L is the length of the ring.

The length of the ring must be an integral number of guide wavelengths of coupled wave, which will reinforce previously coupled energy and place the ring in a state of resonance [3].

DESIGN OF KEY COMPONENTS

P-band TWRR without DUTs consists of a main directional coupler with a coupling coefficient of C = –10 dB that has low reflection, a directional coupler for power detection(C=-60dB,the directivity $S_{41} - S_{21}$ is better than 30 dB) and 4 H-bents(S_{11}<-50dB@650MHz). The 3 key components parameters calculated by CST MWS[4] are presented in figure 3.

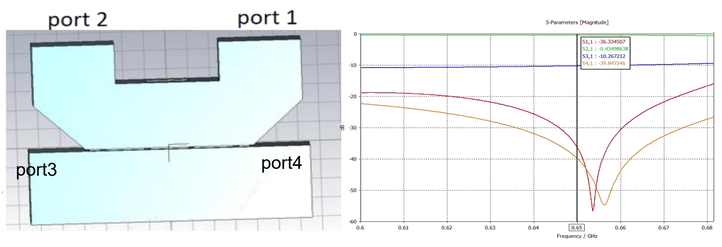

(a)Main directional coupler

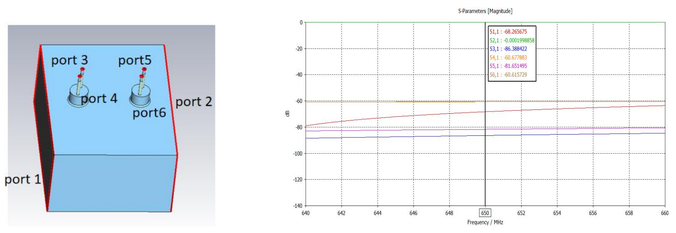

(b)Directional coupler for power detection

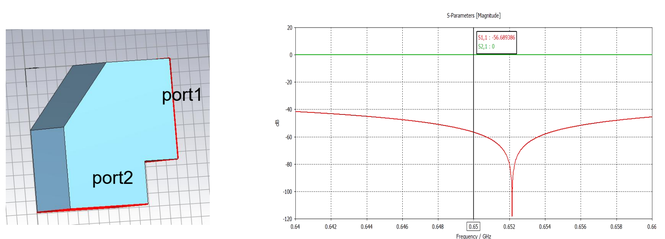

(c)H-bent

Figure 3 Design of 3 Main Components

P-BAND TWRR DESIGN

Configuration of P-band TWRR is showed in figure 4 and figure 5.The theritical maximal power gain M_{max}=36.7.

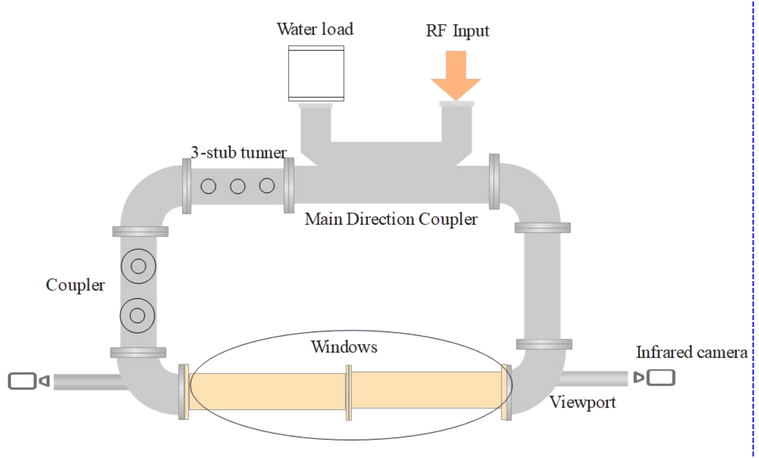

Figure 4 Configuration of P-band TWRR

The direction of power flow inside the P-band TWRR is showed in figure 5.

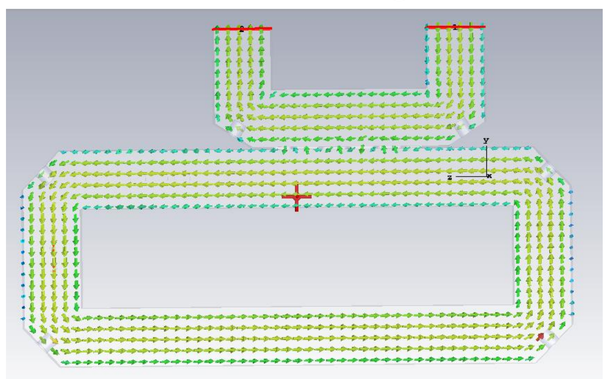

Figure 5 Power flow in P-band TWRR

P-BAND TWRR DESIGN(Continued)

Figure 6 shows the P-band TWRR model in CST .The maximum power gain of the P-band TWRR is 35.9@ 650 MHz.

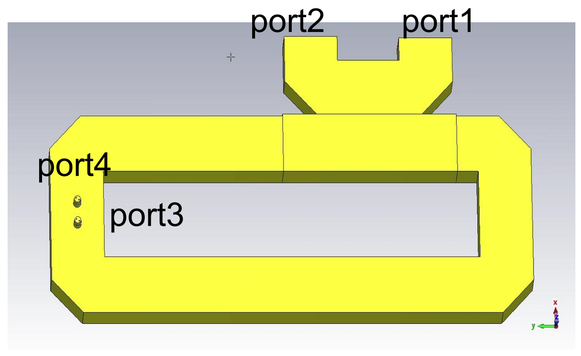

Figure 6 P-band TWRR model

The parameters of P-band TWRR is showed in table1.

Table 1 Results of P-band TWRR

Waveguide	WR1500
Length of the ring	9.28m
Insertion loss of windows	0.05-0.3dB
Coupling coeficeent	–10dB
Power Gain$_{therectical}$	36.7
Power Gain$_{simulation}$	35.9

The maximum temperature rise of the P-band TWRR is 38℃, showed in figure7.

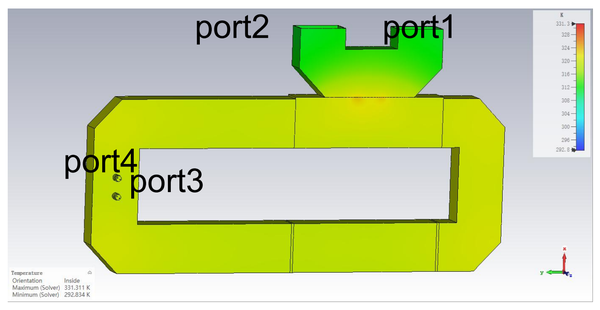

Figure 7 Temperature Rise of P-band TWRR

SUMMARY AND OUTLOOK

This paper presents the development of a 1.2 Mega-Watt P-band TWRR. The main directional coupler is -10dB. The power gain is analyzed theoretically to be 36.7, the simulated value is 35.9 and the maximum temperature rise is 38℃. Next, we will complete the design of the three-stub tuner,along with a phrase shifter. And then the processing of P-band TWRR will be undertaken..

REFERENCES

[1]Gao, J. CEPC Technical Design Report: Accelerator. Radiat Detect Technol Methods 8, 1–1105 (2024). https://doi.org/10.1007/s41605-024-00463-y

[2]"Theory and Application Instruction Manual for the Resonant Ring" I-T-E Circuit Breaker Company, Special Products Division, Philadelphia 34, Pennsylvania.

[3]Resonant Ring for High Power Tests of RF Couplers, Veshcherevich, Vadim.,Physics, Engineering,2003.

[4]CST GmbH, Darmstadt, Germany.

* Work supported by Yifang Wang's Science Studio of the Thousand Talents Project

† email address: zhouzs@ihep.ac.cn

B08

Electromagnetic and Quench Characteristics of the CEPC Detector Superconducting Magnet

Menglin Wang[1], Feipeng Ning[1], Ling Zhao[1], Zhilong Hou[1] , Yatian Pei[1] , Yingshun Zhu[1] , Jieru Geng[1] , Qingjin Xu[1]

[1]Institute of High Energy Physics (IHEP), Chinese Academy of Sciences (CAS), Beijing, China

中国科学院高能物理研究所 Institute of High Energy Physics Chinese Academy of Sciences

Introduction

CEPC Detector Superconducting Magnet

- **Coil: 4 layers *700 turns, center field 3T@17kA**
- **Cable: Al-stabilized NbTi/Cu Rutherford cable, double-coated aluminum Box type**
- **Cooling: Thermosyphon cooling method with a small temperature difference, the operating temperature is 4.2K**
- **Support: Suspension system composed of titanium alloy rods**
- **Quench protection: Based on the dump resistor**

Layout and parameters

Parameters	Value	units
Coil Inner diameter	7300	mm
Coil Outer diameter	7916	mm
Coil length	8150	mm
B@(0,0,0)	3 T	T
Operating current	17	kA
Coil Module gap	50	mm
Inductance	11	H
Stored Energy	1.54	GJ
Cable dimension	56*22	mm
Number of strands	32	
Coil length	8150	mm
Cable critical current@4.2 K, 5 T	51	kA

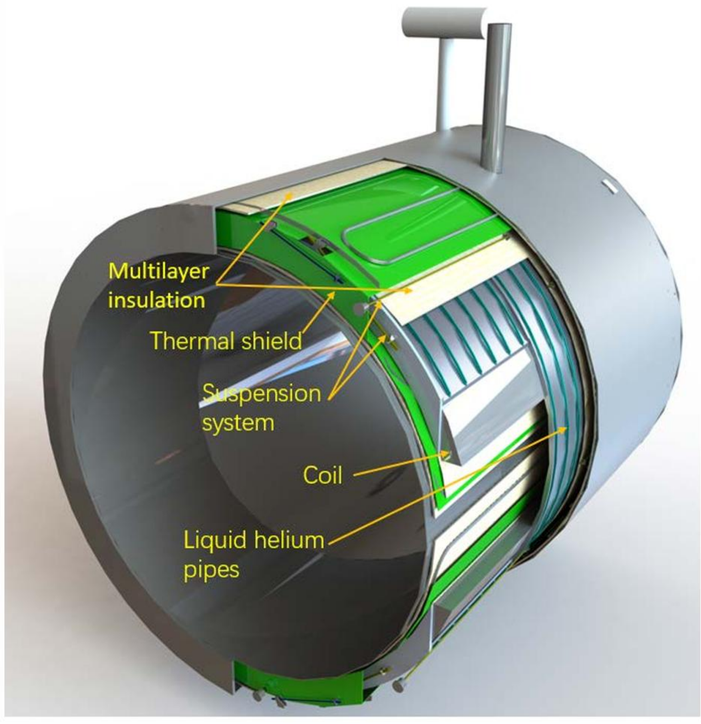

Magnetic field design

- **Detector magnet: Solenoid: B_{center} is 3 T, B_{peak} in coil is 3.8 T**

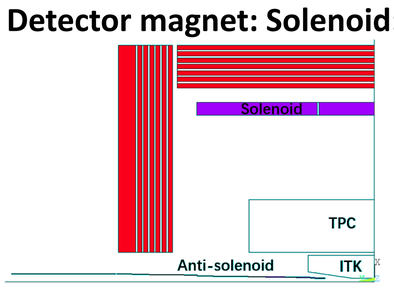

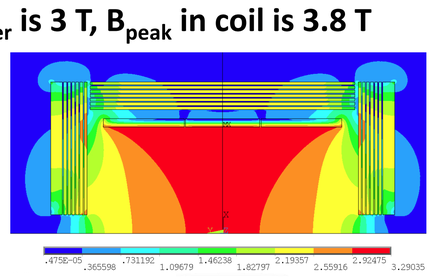

- **Yoke**

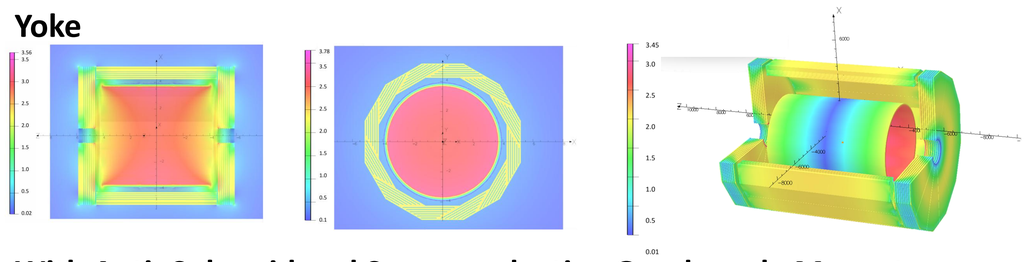

- **With Anti- Solenoid and Superconducting Quadrupole Magnet**

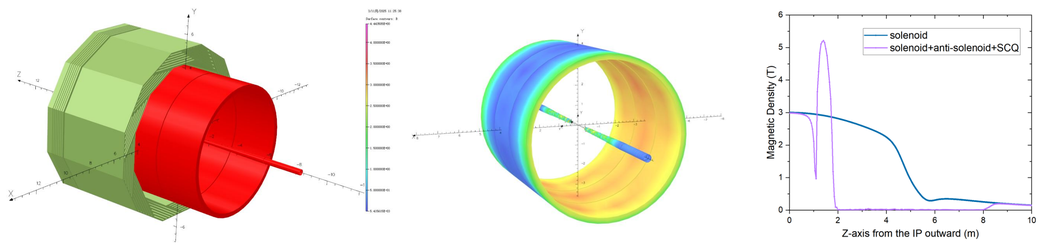

- **Stray field**

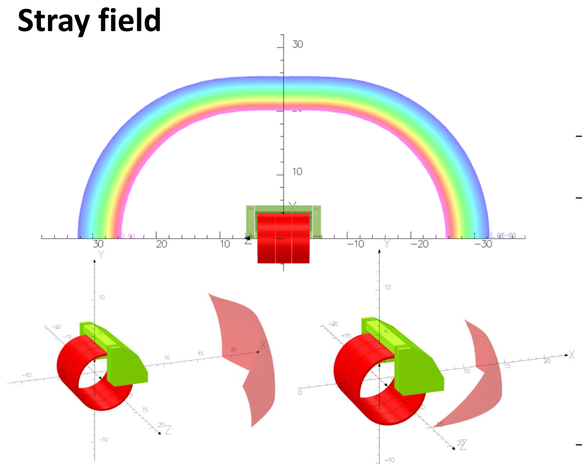

Stray field		Position
50 Gs	R direction	25.4 m
	Z direction	32.3 m
100 Gs	R direction	20.2 m
	Z direction	25.6 m

- **Field Uniformity in TPC region**

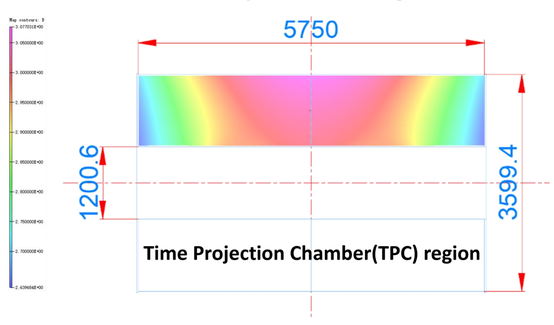

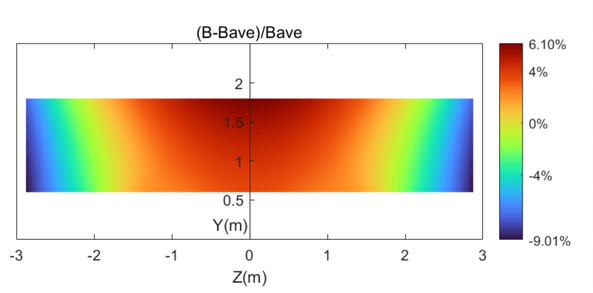

Quench Characteristics

Quench detection and protection

- **Quench detection： Voltage of the coil**
- **Quench protection： dump resistor + quench back cylinder**

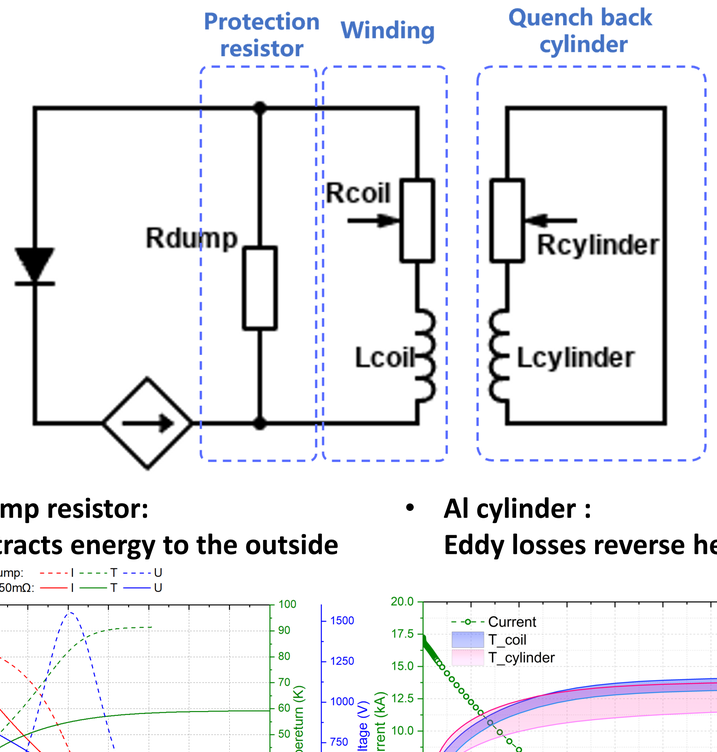

- **Dump resistor: Extracts energy to the outside**

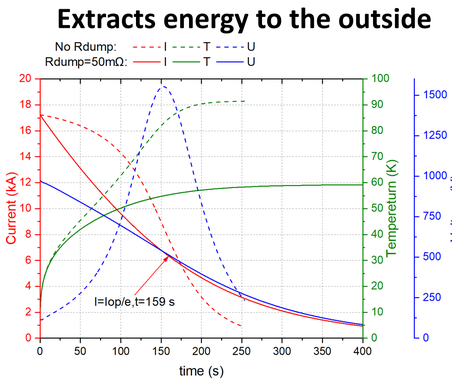

- **Al cylinder : Eddy losses reverse heating coil**

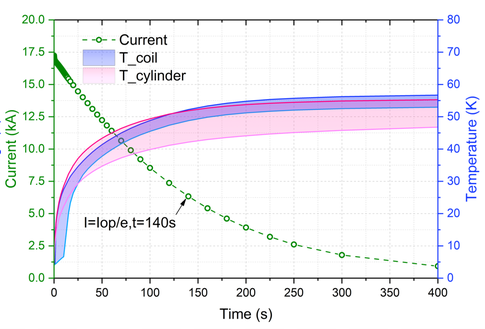

Quench parameters

- **The RRR of the Al stabilizer: > 600 is better**

- **Minimum energy energy and quench propagation speed**

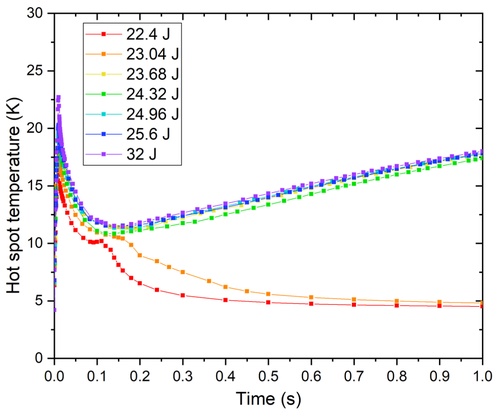

- **Along the cable: 2.514 m/s**
- **Axially: 0.089 m/s**
- **Radially: 0.139 m/s**
- **MEQ: ~24.96J**

- **The coil temperature after quenching triggered from the innermost turn**
  - **With Dump resistor and quenchback cylinder, delay time = 0 s**

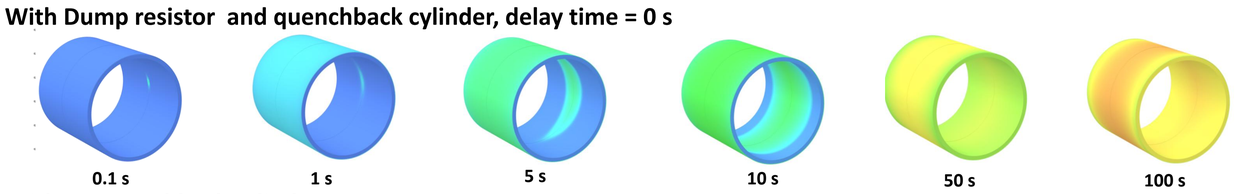

  - **With no quenchback cylinder**

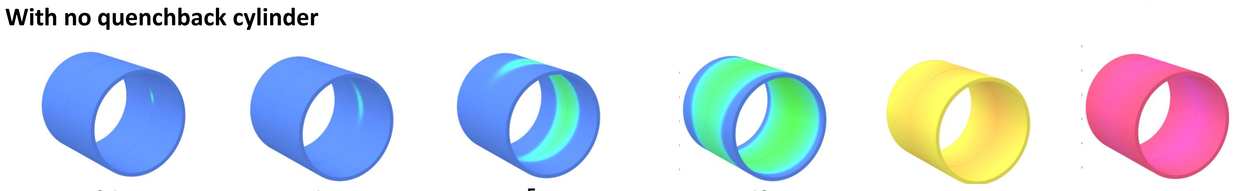

Email: wangmenglin@ihep.ac.cn

Poster ID: #78 The 2025 International Workshop on the High Energy Circular Electron Positron Collider (CEPC2025), Guangzhou, China, Nov 5 – 10, 2025

Reliability Design for High Power RF Source Systems in Large Particle Accelerators

B09

LIU J.D, Zeng Y.L, Shi X.Q, Li F, ZHOU Z.S, He D.Y, He X, Li X.P, Meng C, LI J.Y

1. Institute of High Energy Physics, Chinese Academy of Sciences, Beijing, China
2. University of Chinese Academy of Sciences, Beijing 100049, China

liujd@ihep.ac.cn, zhouzs@ihep.ac.cn

INTRODUCTION

The RF power source system is a critical component of the CEPC, providing the high energy required to accelerate positrons and electrons in order to compensate for energy losses due to synchrotron radiation and interactions between the beam and cavity impedance. Its reliability and stability directly affect the operational efficiency of the entire facility. Based on operational experience from existing facilities, the RF power sources, due to their high power, high voltage, and active equipment characteristics, consistently exhibit high failure rates during long-term operation across all systems. Therefore, for future advanced particle accelerators, which will incorporate large clusters of RF power sources characterized by numerous devices distributed over wide areas, enhancing long-term operational reliability will pose a significant challenge and is a common issue faced by all accelerator facilities today. This paper summarizes the challenges faced, design approaches, and the processes involved in the development and testing of prototypes, providing a technical reference for achieving high reliability in large particle accelerators.

Over recent years, IHEP has developed various types of RF power sources based on particle accelerator projects, including:

A） Microsecond-level RF power sources

characterized by pulse widths of several microseconds. The pulse modulator delivers peak power at the hundred-megawatt level, with average power ranging from 10 kW to 100 kW. Solid-state modulators offer the distinct advantage of high repetition rate stability (up to 17.2 ppm).

B）Hundred-microsecond-level RF power sources

featuring long pulse widths (100 μs to 10 ms). The pulse power supply provides peak power from hundreds of kilowatts to 10 MW. Key characteristics include flexible pulse width modulation (with programmable pulse leading/trailing edges and pulse width) and high repetition rate stability (up to 107 ppm).

C） Long-pulse/Continuous-wave (CW) RF power sources

distinguished by megawatt-level average power output. These systems are characterized by high power, low ripple, and long-term stability (0.1% at megawatt-level power output).

For future large-scale particle accelerator projects, their high-brightness targets necessitate the integration of hundreds of diverse RF power source systems. These systems feature high power levels (up to the hundred-megawatt range) and widespread distribution (covering a broad power range). For such a large-scale installation, high-reliability design is crucial for ensuring the high availability of the accelerator.

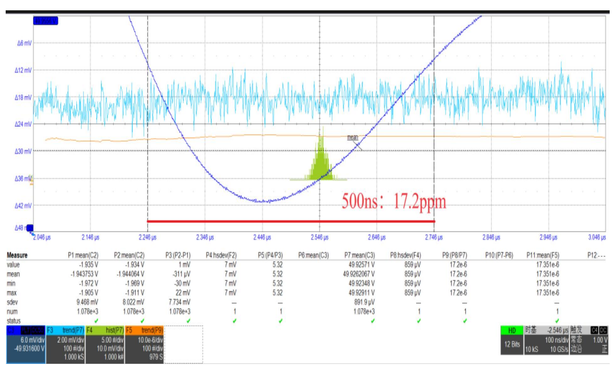

A) Microsecond-level（<10μs） pulse modulator

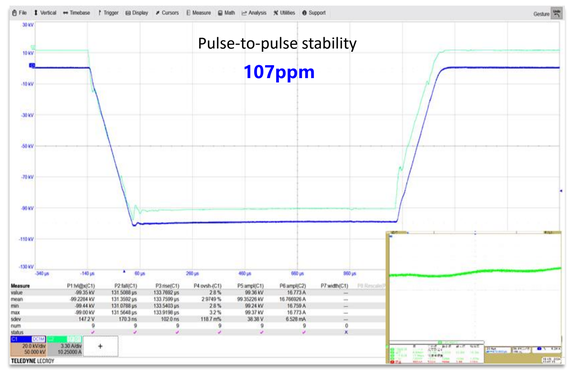

B) Long pulse (100μs-10ms) RF pulse power source

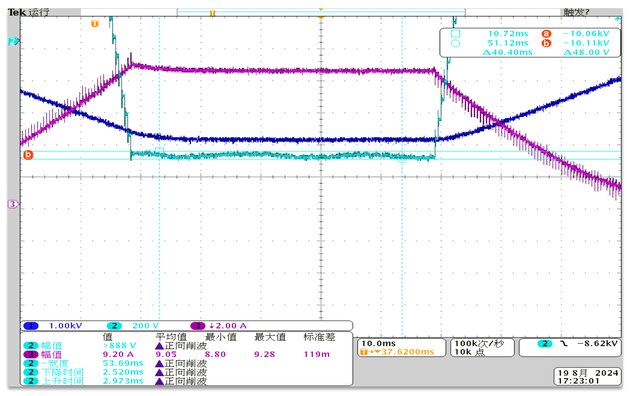

C) Long pulse (50ms) RF pulse power source

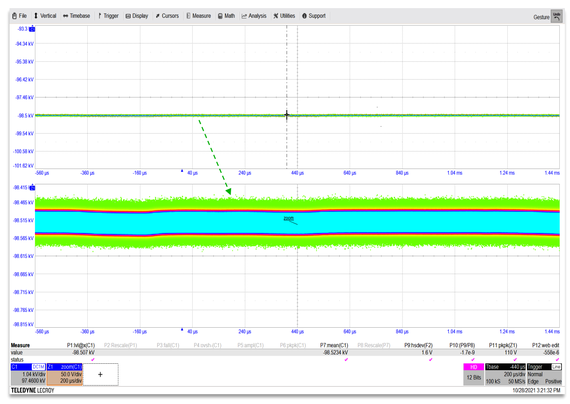

D) CW RF pulse power source

RF power sources with different pulse modes developed by IHEP team

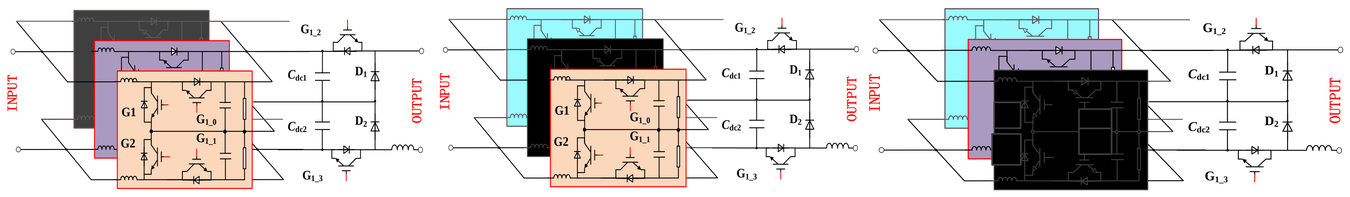

- **Megawatt-level HVPS**
- **High Voltage coaxial cable Long distance transmission**
  - Cable length >150m
  - High Voltage Connectors
- **Tunnel Cabinet**
  - High voltage adapter
  - Filament, Mod-Anode, Focusing PS
  - arcing energy suppression
  - Interlocks and Controls
- **Beam line**
  - High efficiency klystrons
  - Transmission Waveguide
  - Superconducting Cavity

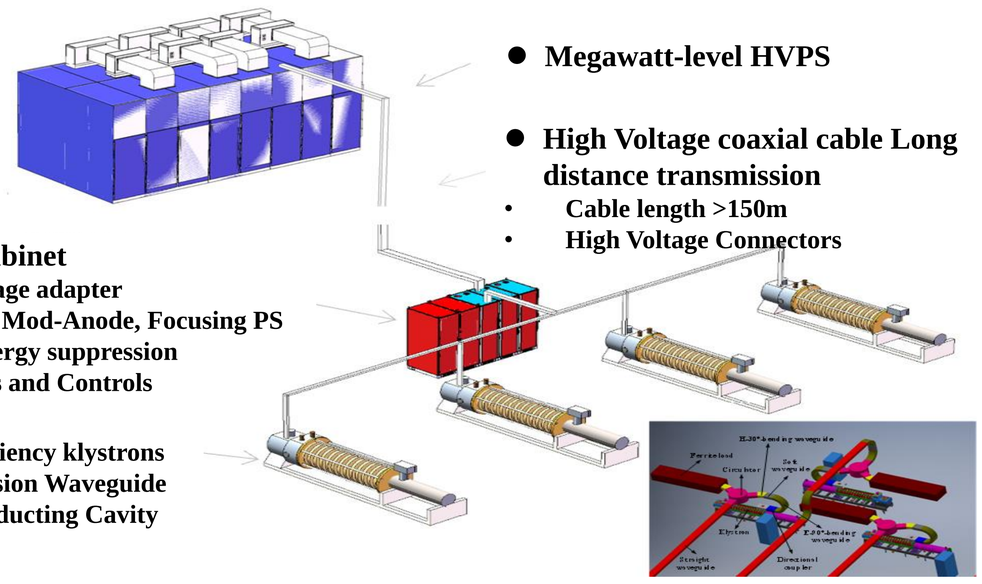

RF Power System Megawatt-level HVPS to Klystron with 1 to 2 or 1 to 4 Layout Schematic

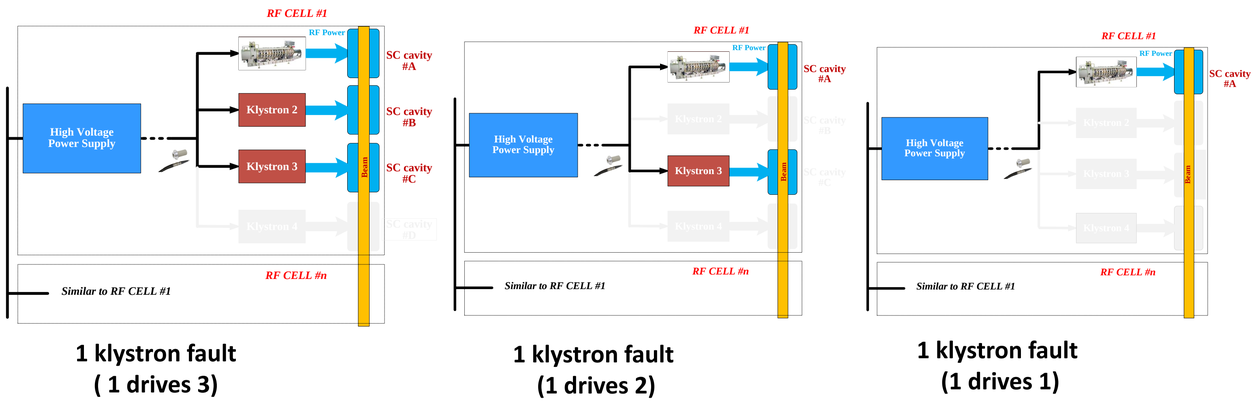

1 klystron fault (1 drives 3)

1 klystron fault (1 drives 2)

1 klystron fault (1 drives 1)

➢ **Fault-tolerant control (Klystron load):** 1-to-4, 4 klystron can be selectively redundant (standby, operation maintenance, etc.). The engagement and disengagement of the load of a single or several fast regulation pipes, and the stability/protective logic control of the high-voltage power supply system.

➢ **Fault-tolerant control (unit modules):** Multiple redundancies, mutual redundancy between power branches; a single path failure does not affect the system's high-voltage output. Redundant control between unit modules ensures the reliability of cascaded high-voltage DC output.

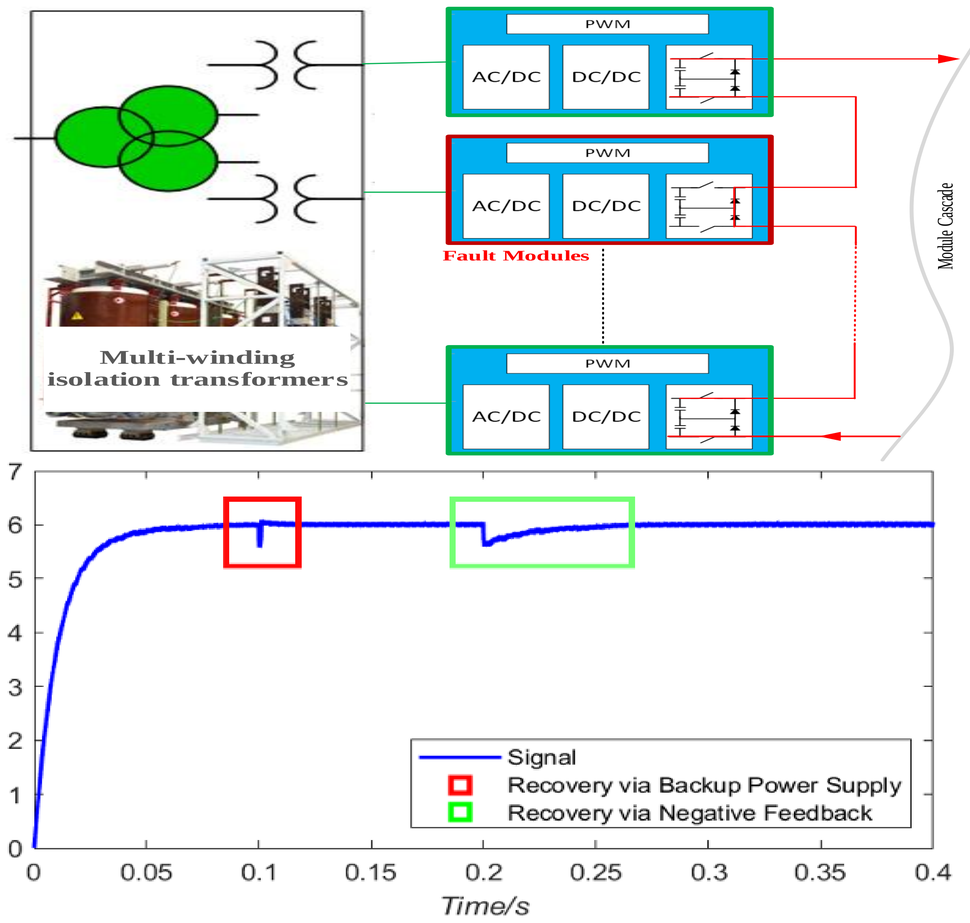

➢ **Fault-tolerant control (system level):** A failure of a unit module does not affect the high-voltage/microwave power output at the system level, ensuring the stable operation of the system.

➢ A combination of closed-loop feedforward and feedback comprehensively enhances the system's anti-interference capability and dynamic performance.

➢ **Overall Output Voltage Ripple Comparison (Ripple expected in the order of 0.01% level, 1% for conventional HVPS)**

REFERENCE

[1] Gao, J. CEPC Technical Design Report: Accelerator. Radiat Detect Technol Methods 8, 1–1105 (2024). https://doi.org/10.1007/s41605-024-00463-y

[2] Zhou, ZS., Xiao, OZ., Liu, JD. et al. CEPC RF power sources at TDR. Radiat Detect Technol Methods 9, 429–442 (2025). https://doi.org/10.1007/s41605-025-00523-x

The future research supported by National Natural Science Foundation of China (Grant No. 12205320, Grant No.12275288) ; Work also supported by PAPS project and Yifang Wang's Science Studio of the Thousand Talents Project.

B10

Optimization of Cavity Shape for C-Band Accelerating Structure

Rao. Ghazal, JR. Zhang, OZ. Xiao, C.Meng
IHEP-UCAS, Beijing, China

中国科学院高能物理研究所
Institute of High Energy Physics
Chinese Academy of Sciences

INTERNATIONAL WORKSHOP
ON THE HIGH ENERGY CIRCULAR ELECTRON POSITRON COLLIDER
CEPC 2025
November 6-10, 2025 Guangzhou, China

Background. **The baseline design for the CEPC linac has been established at 30 GeV, employing S-band and C-band normal-conducting accelerating structures (AS). From 1.1GeV to 30GeV after the damping ring, there are 235 sets C-band units with pulse compressors. A C-band high-power test bench will be established in Huairou Park at IHEP.**

RF Distribution of 30 GeV linac

S-band, 80 MW klystron, S-band structures: 93, big hole S-band structure after the positron source is 16, with 33 pulse compressors.

- 1-1(ESBS), 1 accelerating structure, 22MV/m
- 1-4 (FAS), 21 sets, 84 standard accelerating structures, with pulse compressor, 22MV/m
- 1-2(PSPAS), 8 sets, 16 big hole accelerating structures, 22MV/m, with pulse compressor
- 1-2(SAS), 4 sets, 8 accelerating structures, 27MV/m , with pulse compressor

C-band, 50 MW klystron, C-band structures: 470, with 235 pulse compressors.

- 1.1GeV-30GeV, 1-2(TAS), 235 sets, 470 accelerating structures, ~40MV/m

Introduction of RF System

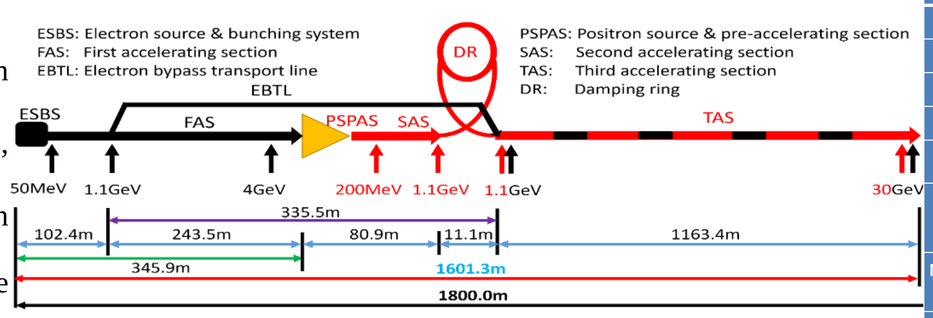

Specifications of the structure

Parameter	Unit	S-band		C-band
Frequency	MHz	2860		5720
Length	m	3.1	2.0	1.8
Cavity mode		2π/3		3π/4
Aperture	mm	19~26	25	12~16
Gradient	MV/m	22/27	22	40
Cells (include coupler cells)		86	55	89
Number of Accelerating Structure		93	16	470
Number of Klystron		33		236
Klystron Power	MW	80		50

Optimization of Cavity and Iris Geometries

This study focuses on optimizing the cavity shape of a C-band accelerating structure to achieve a higher shunt impedance while maintaining a low normalized surface electric field (Es/Eo).Several cavity geometries and iris configurations were designed and analyzed using Superfish, and their performance results were compared. Among the examined models, an elliptical racetrack-type pillbox cavity with an elliptical iris was identified as the most effective design, providing improved field distribution and enhanced RF efficiency. A parametric study on thickness (t) was also performed. Based on the balance between shunt impedence and Es/Eo, an optimal thickness of 4mm was selected. The optimized geometry was further validated through CST Studio Suite simulations, confirming the consistency and accuracy of the design results.

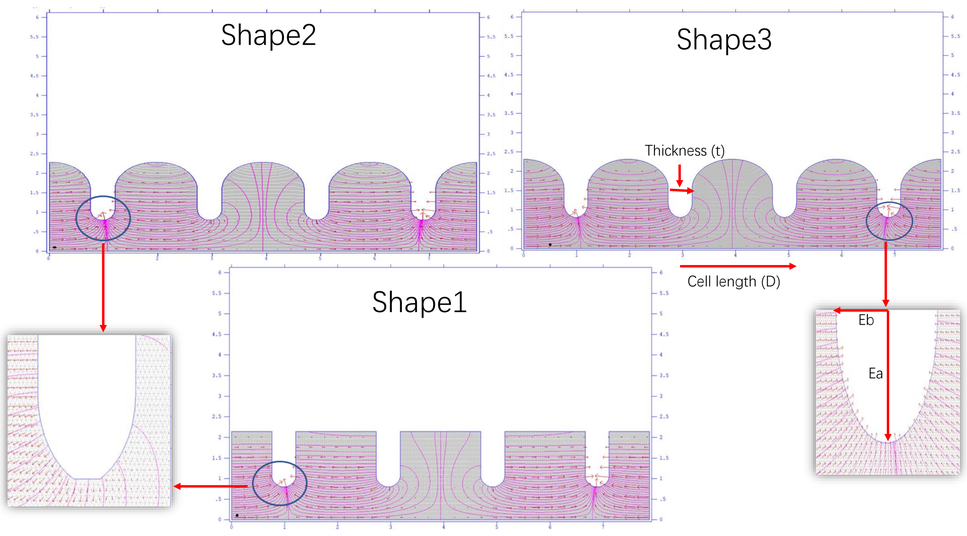

Shape 1 (Q=10110, R=60.504, Emax/Eo=3.0656)
Shape2 vs Shape 1
Q: +11.89%, R: +9.76%, Emax/Eo: −2.11% → "Q factor increase more than 11.9%, shunt impedence increase 9.8%, Emax/Eo decreases by 2.1%."
Shape 3 vs Shape 1
Q: +12.28%, R: +10.61%, Emax/Eo: −7.37% → "Q factor increase more than 12%, shunt impedence increase 10.6%, Emax/Eo decreases by 7.4%."

Three cavity iris profiles (Shapes 1-3) investigated how geometric variation affects shunt impedance(R), Q-value, and normalized surface field (Emax/E0) under identical operating conditions that are Thickness (t) =4.5mm, Phase advance/cell=3π/4, Cell length (D) = 19.682mm.

Parametric Optimization of Iris Ellipticity, Thickness, and Phase Advance/Cell for Cavity Design

At Iris Ellipticity=1.6 , Frequency=5.712MHz, elliptical iris tip

Frequency=5.712MHz,elliptical iris tip

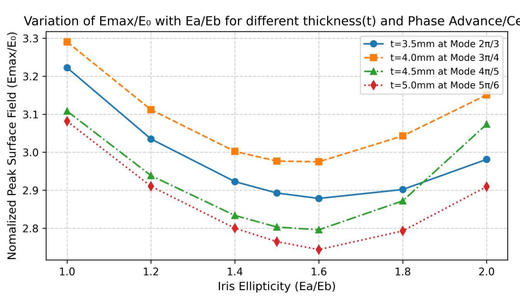

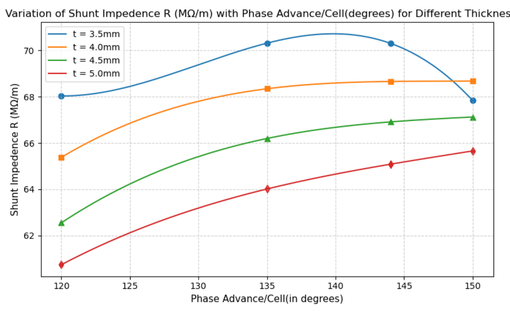

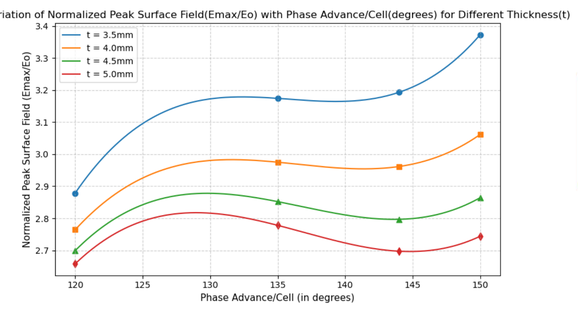

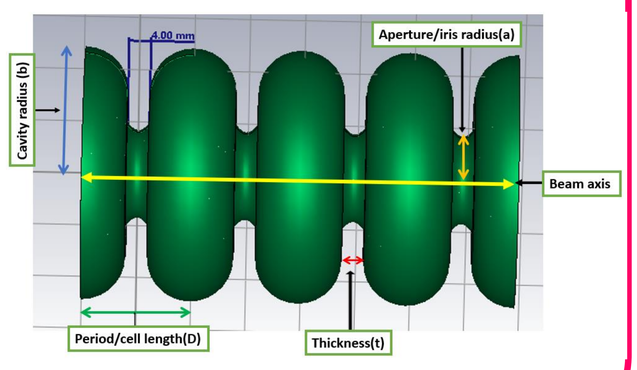

Iris Ellipticity(Ea/Eb) was varied from 1.0 – 2.0 with Thickness (t) = 3mm – 5 mm and modes from 2π/3 to 5π/6 and the results on this show that the Ea/Eb = 1.6 provides the highest shunt impedance (R) and lowest normalized surface field (Emax/E0).
Then with Ea/Eb = 1.6, the iris thickness was varied from 3.5mm to 5mm across different modes to study the influence on R, and Emax/E0. The analysis confirms that t ≈ 4 mm offers good results

Validation and Wakefield Analysis of Optimized Unit Cell

At t=4mm, Iris Ellipticity=1.6, frequency=5.712 MHz, elliptical iris tip

Operating Mode	Cell length D(mm)	Quality Factor Q	Surface Electric field Emax/Eo	Shunt Impedence R(MΩ/m)	Coupling coefficient k	Group Velocity Vg/c	Attenuation factor(τ)	Filling time tf(ns)	Phase Stability (°/MHz)
2π/3	17.495	10446.9	2.764	65.38	0.0366	0.0341	0.08822278	3.26004	0.0112
3π/4	19.682	11567	2.975	68.34	0.0326	0.0281	0.09668826	3.95593	0.0154
4π/5	20.988	12197	2.961	68.66	0.0304	0.0233	0.11045103	4.76516	0.0198
5π/6	21.8686	12606	3.061	68.67	0.0291	0.0198	0.12612714	5.62394	0.0244

Validation check at Frequency=5.712MHz, t=4mm, Phase Advance/cell= 3π/4 , elliptical iris tip

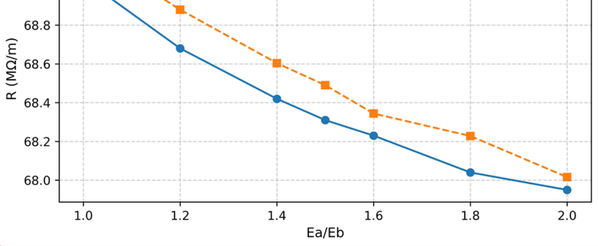

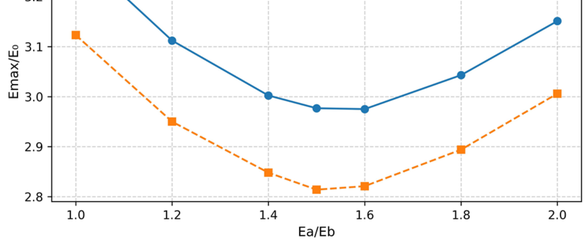

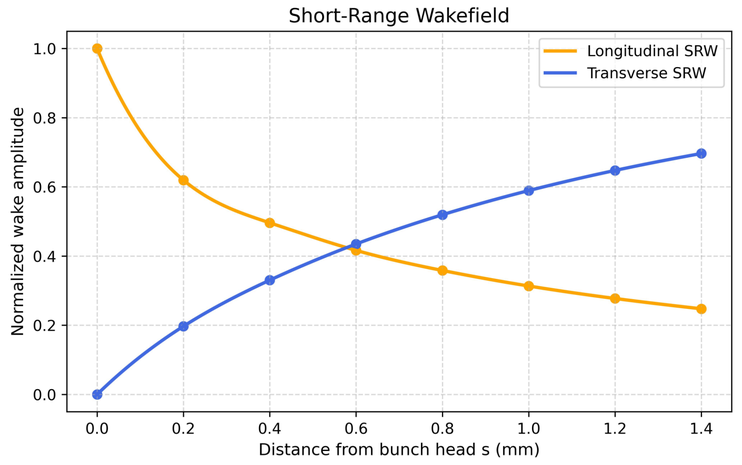

Consistency of the optimized results was verified through CST and Superfish simulation that shows close agreement in Shunt Impedence R, and Emax/Eo whereas CST is used to optimize the single cell in eigenmode default set (1J stored energy in the cavity).
Shunt Impedence: 0.10 % – 0.30 %
Emax/E₀: 4.6 % – 5.5 %

References

[1]. Dolgashev, V. A. (2021). Design criteria for high-gradient radio-frequency linacs. Applied Sciences, 11(9), 4116. MDPI. https://doi.org/10.3390/app11094116
[2]. Bane, K. L. F. (2003, March 4). Short-range dipole wakefields in accelerating structures for the NLC (SLAC-PUB-9663; LCC-0116). Stanford Linear Accelerator Center, Stanford University.
[3]. Fang, W. C., Gu, Q., Tong, D. C., & Zhao, Z. T. (2011, January). Design and experimental study of a C-band traveling-wave accelerating structure. Chinese Science Bulletin, 56(1), 18–23. https://doi.org/10.1007/s11434-010-4265-2
[4]. Fang, W. C., Gu, Q., Tong, D. C., & Zhao, Z. T. (2011, November). Design optimization of a C-band traveling-wave accelerating structure for a compact X-ray Free Electron Laser facility. Chinese Science Bulletin, 56(32), 3420–3425. https://doi.org/10.1007/s11434-011-4754
[5]. Bane, K. L. F., Wang, J., Raubenheimer, T. O., Ruth, R. D., & others. (2001, February). Traveling wave structure optimization for the NLC. In Proceedings of the 2001 Particle Accelerator Conference (PAC 2001). IEEE. https://doi.org/10.1109/PAC.2001.986135

中國科學院高能物理研究所
Institute of High Energy Physics
Chinese Academy of Sciences

RF design of a C-band spherical cavity pulse compressor

OZ. Xiao, JR. Zhang, C.Meng, HJ. Cao

IHEP, Beijing, China

INTERNATIONAL WORKSHOP
ON THE HIGH ENERGY CIRCULAR ELECTRON POSITRON COLLIDER
CEPC 2025
November 6-10, 2025 Guangzhou, China

Abstract. **The baseline design for the CEPC linac has been established at 30 GeV, employing S-band and C-band normal-conducting accelerating structures (AS). From1.1GeV to 30GeV after the damping ring, there are 235 sets C-band units with pulse compressors. A C-band (5712 MHz) spherical cavity pulse compressor have been developed, the TE_{114} mode with an unloaded Q factor of 126,000 is selected for resonance in the spherical cavity, and the energy multiplication factor of the entire pulse compressor is 2 with the coupling coefficient of 5.43, and the peak power gain can exceed 6.**

Introduction

The pulse compressor enhances the performance of accelerators by increasing the radio frequency (RF) peak power. Since the SLAC Energy Doubler (SLED) system first proposed and applied this technology in 1974, various types such as Binary Pulse Compression (BPC) and Resonant Line SLED (SLED-II) have been gradually developed. The spherical cavity pulse compressor is a variant of the SLED type.

Our compressor comprises a special 3dB coupler and a single spherical energy storage cavity. The special 3dB coupler converts the TE_{10} mode in the rectangular waveguide into two polarization degenerated TE_{11} modes in the cylindrical waveguide; it also acts as a circular polarizer, with a 90° phase difference between the two TE_{11} modes. The TE_{114} mode with an unloaded Q factor of 126,000 is selected for resonance in the spherical cavity, and the energy multiplication factor of the entire pulse compressor is 2 with the coupling coefficient of 5.43, and the peak power gain can exceed 6. The table on the right presents the main parameters of the pulse compressor. Compared with traditional SLED-type pulse compressors, the spherical cavity pulse compressor achieves pulse compression using only one spherical cavity, leading to a compact overall structure.

Parameter	value	Units
Working frequency	5712	MHz
Working mode	TE_{114}	----
Cavity Radius	116.88	mm
Input pulse length	3	μs
Output pulse length	0.35	μs
Coupling coefficient (β)	5.43	----
Unloaded Q	126000	----
Energy multiplication factor	2	----
Peak power gain	> 6	----

Main Specifications of the structure

Special 3dB coupler design

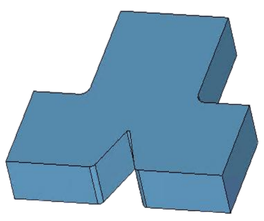

Two-port T-shaped waeguide model diagram

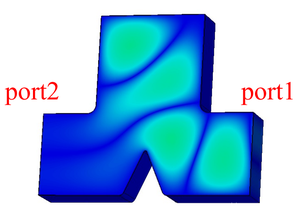

Two-port T-shaped waveguide electric field diagram

- In the two-port T-type waveguide, our design satisfies the direct reflection of the wave input from Port 1 and no output from Port 2. Additionally, the overmoded waveguide section is designed. Using the cutoff wave number formula and combining the mode distribution diagram of the rectangular waveguide,the value range of the wide side of the overmoded waveguide of the T-type waveguide is determined so that it only transmits the TE_{10} mode and the TE_{20} mode.

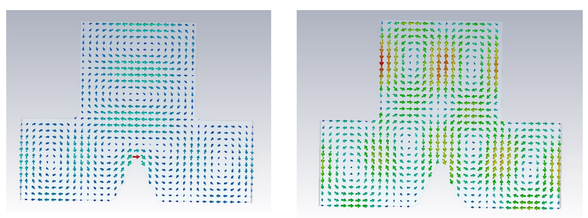

Waveguide modes in a T-shaped waveguide: TE_{10} on the left, TE_{20} on the right

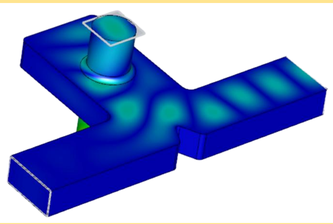

Electric field diagram of the mode converter

- Attachment of a cylindrical waveguide to the T-type waveguide yields a complete 3-dB coupler. The determination of the cylindrical waveguide's radius range is first performed: through the combination of its mode distribution and electromagnetic wave propagation conditions, the design requirement is derived—TE_{11} mode transmission with TM_{01} mode cutoff, namely $\lambda c(TM_{01}) < \lambda < \lambda c(TE_{11})$. The positioning of the cylindrical waveguide is then fixed to maximize the output of the input power from Port 3 (at the cylindrical waveguide), thereby ensuring the two output TE_{11} modes exhibit equal amplitude and a 90° phase difference.

Design of spherical energy storage cavity

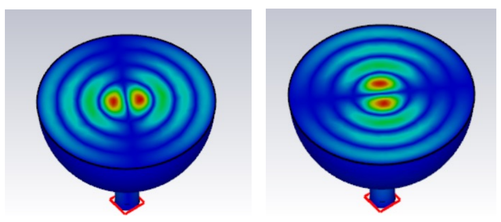

Working mode of the spherical cavity the two TE_{114} modes

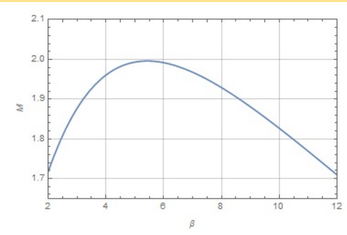

The variation trend of the energy multiplication factor with respect to the coupling coefficient

Smith chart of spherical resonator (over-coupled)

$$\beta = \frac{1+|S21|}{1-|S21|}$$

Relationship between the coupling coefficient and |S21|

- Electromagnetic oscillations in a spherical cavity are a passive electromagnetic field problem, with their solution reducible to solving the vector Helmholtz equation (below):

$$\nabla^2 \boldsymbol{E} + k^2 \boldsymbol{E} = 0$$
$$\nabla^2 \boldsymbol{H} + k^2 \boldsymbol{H} = 0$$

- For the cavity's operating modes, applying the zero tangential electric field boundary condition and spherical coordinate electromagnetic components yields the relationship between spherical radius and Bessel function roots across modes, with the TE114 mode radius calculated as 117.5 mm. For the cavity's TE modes, the unloaded Q-factor depends solely on radius (126000 at this radius). Substituting other key technical parameters of structure into the formula (below):

$$M = \gamma e^{-T_a/T_c}[1-(1-g)^{1+\nu}][g(1+\nu)]^{-1} - (\alpha - 1)$$

yields the energy multiplication factor's variation with coupling coefficient, and the figure shows the factor peaks at 2.0 when the coupling coefficient is 5.43.

- The simulated Smith chart shows an overcoupling state. The relationship between the coupling coefficient and |S21| is given by the formula in the left figure, from which the required |S21| value is derived, with the coupling coefficient being 5.43 and meeting the design target.

Design of the spherical pulse compressor

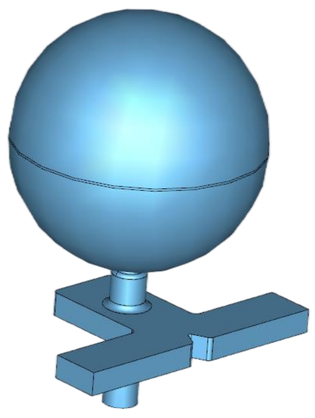

Model diagram of a C-band spherical energy storage cavity pulse compressor

- A spherical resonant cavity and a 3-dB coupler are combined to form a spherical pulse compressor. By converting the TE_{10} mode input into the rectangular waveguide to the TE_{11} mode in the circular waveguide, the spherical resonant cavity is ultimately made to operate in the TE_{114} mode (at 5712 MHz).

- Meanwhile, adding a structure for equatorial enlargement to the spherical cavity enhances mode isolation and facilitates subsequent tuning.

$$V_r'(x) + PV_r(x) = Q$$

Uniform-form first-order linear ordinary differential equation

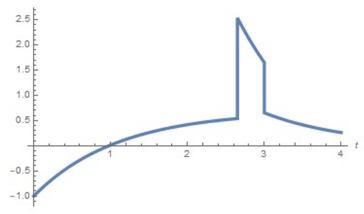

Waveforms of the output E-field

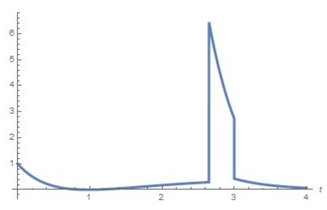

Waveforms of the output power

- The study employs the equivalent circuit method to derive the characteristics of this compressor. By representing the resonant cavity with a parallel resonant circuit and through a series of theorems and simplifications, a general first-order linear ordinary differential equation (as shown on the left) is obtained. The output results of the pulse compressor are then determined via piecewise solution and initial values. It can be seen from the "Waveforms of the output power" figure that the peak power gain reaches a maximum value of 6.45.

The C-band (5712 MHz) spherical cavity pulse compressor converts the TE_{10} mode input from the port into two polarization-degenerate TE_{11} modes through this special 3 dB coupler, which satisfies the conditions of equal amplitude and a 90-degree phase difference. These modes then enter the spherical resonant cavity, where the cavity selects TE_{114} as the operating mode. The energy multiplication factor can reach 2, and the peak power gain can exceed 6.

Research on Scalable NEG Coating Techniques for CEPC Copper Vacuum Chambers : From Lab-Scale to Mass Production

Fei Sun[a], Yongsheng Ma[a,b], Tao Huang[a], Yuchen Yang [a], Baiqi Liu[a,b], Dizhou Guo[a], Haiyi Dong[a], Ping He [a,b]

[a]Institute of High Energy Physics, Chinese Academy of Sciences, 19B Yuquan Road, Beijing, 100049, China;

[b]University of Chinese Academy of Sciences, 19A Yuquan Road, Beijing, 100049, China;

*Corresponding authors: Yongsheng Ma (mays@ihep.ac.cn)

B12

Background & Motivation:

- ✓ Ultra-High Vacuum (UHV) Demand: Future circular colliders (e.g., CEPC) require UHV (3×10^{-10} mbar) for positron beam stability.
- ✓ NEG Technology: Non-Evaporable Getter (NEG) films enable distributed pumping and suppress electron cloud effects (lower secondary electron emission vs. stainless steel/copper).

The primary obstacles in scaling NEG coating from lab to industrial production include:

- ☐ Inefficient lab-scale processes for high-volume manufacturing.
- ☐ Coating uniformity and repeatability challenges in mass production.

Innovative Solution: Multi-Chamber Parallel Coating

To address these challenges, we propose multi-chamber parallel NEG coating technology, which significantly enhances production efficiency while ensuring:

- High reproducibility of film properties.
- Consistent performance in large-scale applications.

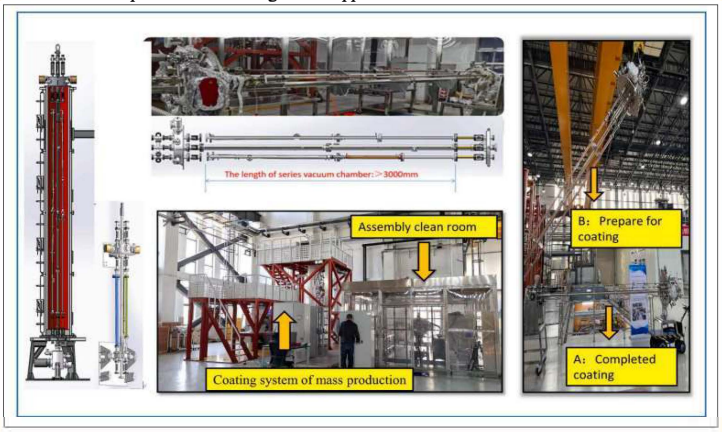

- NEG coating facilities in mass production

Comprehensive Characterization of NEG Films in mass production

➢ Microstructure of NEG films in mass production

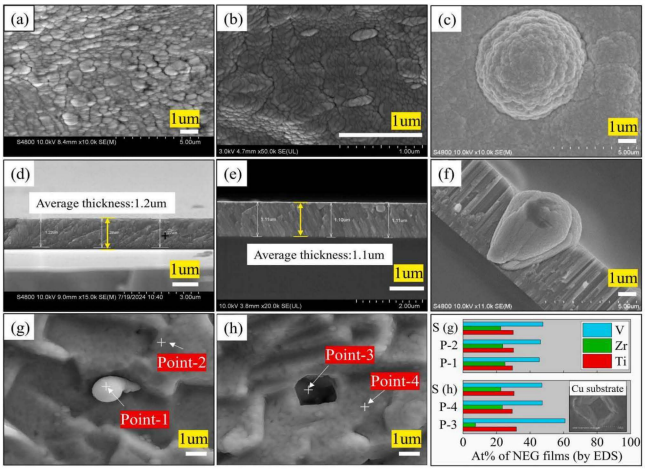

- **SEM:** Porous **columnar microstructure** (~1 μm thick) with intercolumnar porosity (a-b,d–e). **Advantages:** Higher surface area and open **structure enhance gas sorption capacity.**
- **Defect Analysis:** "Protruding particles" (g) and "voids" (h) are observed due to contaminants (dust, micro-arc discharges) and sputtering effects (higher V sputtering yield). **EDS** confirms **defects retain Ti-Zr-V composition** (i), with negligible impact on overall film performance.

➢ Thickness Uniformity & Elemental Composition

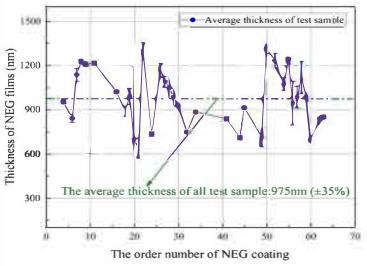

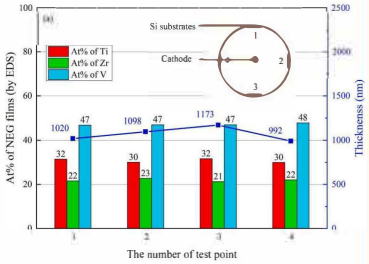

Mass Production Feasibility: Demonstrated high-reproducibility NEG coating of six vacuum chamber assemblies (>3 m total length per assembly) with:

- Uniform thickness distribution (**avg. 975 nm, uniformity <35% across batches**).
- **Stable atomic composition** (Ti-Zr-V) in mass production.

➢ Pumping Speed & Gas Sorption Capacity

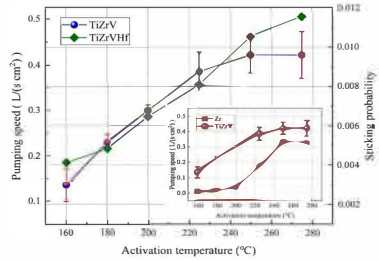

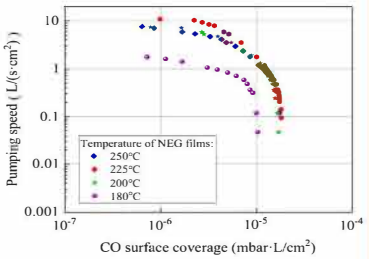

Performance characterization showed temperature-dependent activation dynamics:

- H_2 pumping: 0.48 L/(s·cm²) at 275° C activation.
- CO adsorption: 8.5×10^{-4} mbar·L/cm² at 225° C.

➢ Aging Performance and base vacuum

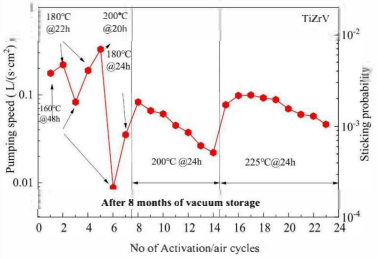

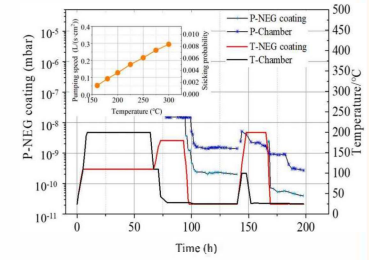

- Lifetime testing showed a 30% per-cycle reduction in sticking probability, aiding maintenance protocols.
- The better base vacuum at the chamber (with NEG) confirms the effectiveness of the NEG films.

Conclusion

This work establishes **a scalable, high-quality NEG coating solution** for future colliders, bridging the gap between lab-scale R&D and industrial production. The technology ensures precise **UHV control**, advancing the feasibility of next-generation light sources and particle accelerators.

Acknowledgments

This work is supported by High Energy Photon Source (HEPS), a major national science and technology infrastructure in China. National Development and Reform Commission (2017) No. 2173

Reference

Y.S.Ma, F.Sun, T.Huang,et al., Research on scalable NEG coating techniques for Cu vacuum chambers in High Energy Photon Source: From lab-scale to mass production, Vacuum, Volume 243, ISSN 0042-207X, https://doi.org/10.1016/j.vacuum.2025.114792.

B13

Absolute Accuracy Improvement of Ring Particle Accelerator Control Network Based on Micron-Level Backbone Network

MA NA[1,2], DONG LAN[1,2], WANG TONG[1,2], LI BO[1,2] , WANG XIAOLONG[1,2] , YAN HAOYUE[1,2], LIAGN JING [1,2] , KE ZHIYONG[1,2] , HE ZHENQIANG[1,2], , LIU XIAOYANG[1,2], LUO PENG[1,2]

1. Institute of High Energy Physics, Chinese Academy of Sciences
2. Spallation Neutron Source Science Center

Introduciton

This paper proposes a scheme for constructing a high-precision straight-overlapping triangular backbone control network. For measuring the height of long sides in large-scale obtuse triangles, an indirect measurement method based on taut wire offset measurement and additional vertex equilateral triangle side length measurement is introduced. Utilizing a self-developed telecentric optical coaxial image offset instrument and its data processing system. For side length measurement, a high-precision concentric measurement scheme based on the μ-base rangefinder is designed. The measurement accuracy of offset distance, long-side height and side length has reached 10μm. This scheme has been deployed and implemented across the entire HEPS storage ring, successfully improving the planar absolute accuracy from 0.13mm to approximately 0.06 mm without compromising the smoothness of the control network, with significant results.

Layout and Accuracy Study of the Straight-Overlapping Backbone Network

1. Backbone Network Layout

The straight triangular backbone network of the HEPS storage ring consists of 39 points, forming a closed backbone network composed of 39 obtuse straight triangles. Each triangle spans approximately 14 segments of the tracker control network. The entire backbone network comprises 78 sides, including 39 long sides and 39 short sides. Constrained by on-site equipment and tunnel structure, the short side lengths range from 30m to 39m, while the long side lengths range from 64m to 72m. The vertex angle corresponding to the long sides is approximately 160°, and the vertical height of the long sides ranges from 2.4m to 3.1m.

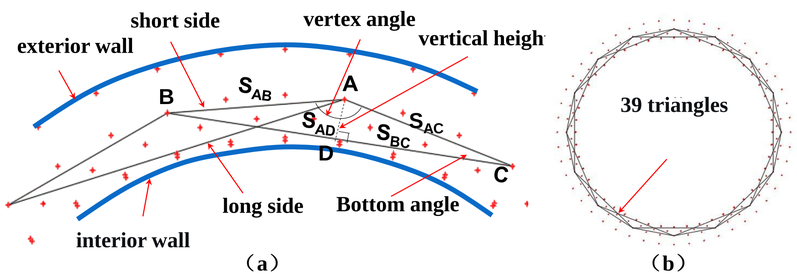

2. Accuracy Simulation Calculation

Based on the triangular backbone network, the functional models for distance observations (Equation 1) and long side height (Equation 2) are established:

$$L_{ik} = \sqrt{(X_i - X_k)^2 + (Y_i - Y_k)^2} \tag{1}$$

$$H_i = \frac{|Ax_i + By_i + C|}{\sqrt{A^2 + B^2}} = \frac{|(y_1 - y_2)x_i + (x_2 - x_1)y_i + x_1y_2 - x_2y_1|}{\sqrt{(y_1 - y_2)^2 + (x_2 - x_1)^2}} \tag{2}$$

Using the adjustment results of 240 station actual observations from the HEPS storage ring as theoretical coordinates, a 240-station tracker observation network was regenerated. The angular observation error σ_{angle} is 0.64″ arcseconds, and the distance observation error σ_{dis} is 0.023mm. Five simulation adjustments were performed by applying different errors to the backbone network side length error σ_L and long side height error σ_H, as detailed in Table 1.

From the radial accuracy σ_r and tangential accuracy σ_t of the adjusted control network, it is evident that merely adding high-precision backbone network side lengths has limited impact on improving control network accuracy. Significant improvement in the ring control network accuracy only occurs when the observation accuracy of the long side height exceeds 0.02 mm.

Table 1 Standard deviation of observations used in simulation adjustments

Scheme	σ_{angle}/"	σ_{dis}/mm	σ_L/mm	σ_H/mm	σ_r/mm	σ_t/mm
1	0.64	0.023	——	——	0.13	0.12
2	0.64	0.023	0.02	——	0.13	0.12
3	0.64	0.023	0.01	——	0.13	0.12
4	0.64	0.023	0.02	0.02	0.10	0.09
5	0.64	0.023	0.01	0.01	0.07	0.06

Backbone Network Measurement Scheme

1. Long Side Height Measurement Using Tension Wire Offset Method

The long side height of the backbone network triangles is obtained indirectly through a scheme based on tension wire offset measurement and additional vertex equilateral triangle side length measurement. As shown in Figure for the measurement content of each triangle: a LEICA AT960 tracker positioned inside the additional vertex triangle △AEF for side length measurement; and a self-designed coaxial image offset instrument set up at base points A, B and additional base points E, F for offset measurement. The RMS for round-trip error of Class 3 measurement is 7μm.

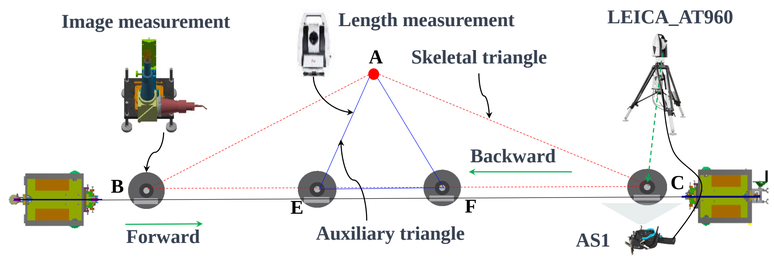

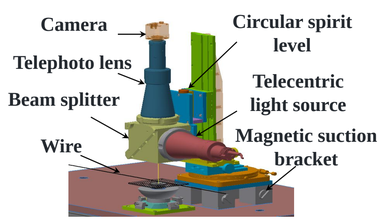

Image offset instrument

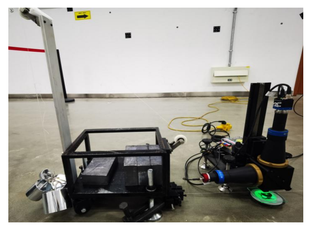

Image measurement

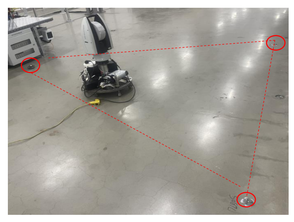

Length measurement

2. Network Side Length Measurement

The LEICA μ-base absolute rangefinder achieves a measurement accuracy of 0.01 mm within a 160m range, serving as a long-distance, high-precision instrument. A concentric measurement scheme has been designed, achieving concentricity among the landmark, measuring instrument, and measurement target:

(1) A 100mm tunnel ball seat landmark designed to ensure concentricity between the landmark center and the μ-base center, effectively avoiding projection errors.

(2) A 100mm to 1.5-inch conversion ball receptacle designed to achieve precise concentricity between the tracker reflector and the 100mm landmark.

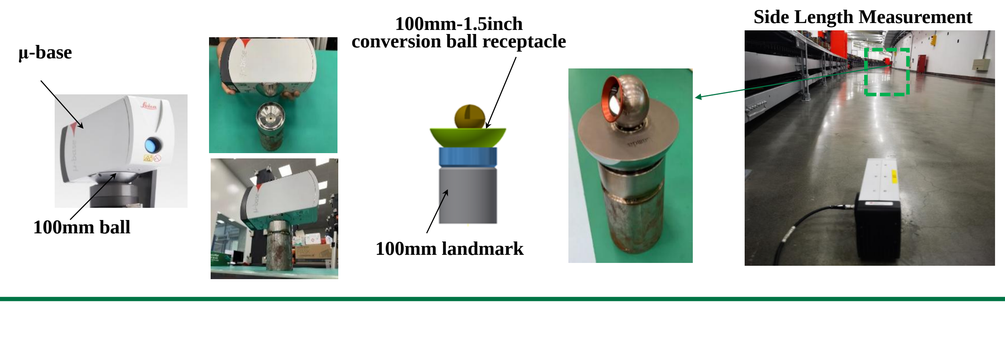

Adjustment Calculation and Results

In February 2025, the HEPS storage ring conducted tunnel control network measurements using a LEICA AT930, along with long side height and side length measurements of the backbone network. Three adjustment schemes were performed:

(1) Independent adjustment of the laser tracker data.
(2) Independent adjustment of the backbone network data.
(3) Integrated adjustment of both laser tracker and backbone network data.

The posterior standard deviation from the three adjustments are shown in Table 2 and the tangential and radial accuracies of network points are presented in Table 3.

Table 2 The posterior standard deviation of observations for three types of adjustment (units: mm, ″)

Laser Tracker		Backbone network		Laser Tracker +Backbone network			
σ_{dis}	σ_{angle}	σ_L	σ_H	σ_{dis}	σ_{angle}	σ_L	σ_H
0.031	0.879	0.011	0.009	0.031	0.878	0.011	0.009

Table 3 Point accuracies and correction values of backbone network observations from the three adjustments (unit: mm).

	Laser Tracker		Backbone network		Laser Tracker +Backbone network			
	σ_r	σ_t	σ_r	σ_t	σ_r	σ_t	V_L	V_H
Max	0.212	0.166	0.114	0.088	0.233	0.115	0.018	0.021
Min	0.000	0.000	0.000	0.000	0.000	0.000	-0.03	-0.027
RMS	0.132	0.122	0.072	0.066	0.065	0.059	0.013	0.012

The adjustment revealed that the backbone network, due to limited redundant observations, is highly sensitive to reliability—accuracy can drop sharply if individual observations contain large errors. From Tables 2and3：

（1）In the independent adjustment of the backbone network, the posterior standard deviations of both the side length and long-side height observations are approximately 10μm; the RMS values of the corrections $V_L$and V_H are also around 7μm. This indicates that the measurement accuracy of the obtuse triangles with a 70m span in the backbone network has reached 10μm；

（2）The radial accuracy σ_r of the storage ring control network improved from 0.132mm to 0.06mm, and the tangential accuracy σ_t from 0.122mm to 0.05mm, doubling the absolute accuracy of the storage ring control network，the effectiveness is remarkably significant .

中国科学院高能物理研究所
Institute of High Energy Physics
Chinese Academy of Sciences

B14

NEG coating and thermal coating spray of vacuum chamber

Yongsheng Ma†, Fei Sun, T Huang, Y. C Yang, D. Z Guo, H. Y Dong, P He

Institute of High Energy Physics, CAS, Beijing, China

Abstract

As the fourth-generation synchrotron radiation light source, vacuum chambers with small apertures were employed for high energy photon source (HEPS), making the performance of Non-evaporable getter (NEG) coating is very crucial for its vacuum system. After years of development, the highly stability of the NEG coating has been achieved. Massive production facilities of NEG coated vacuum chambers have been developed for HEPS in Huairou, Beijing, which based on the NEG coating prototypes. The facilities can achieve simultaneous coating of 16~20 vacuum chambers of HEPS including irregular shaped vacuum chambers. The pumping performance of the NEG coated vacuum chambers has been measured by test facilities. After heated at 200 ° C for 24 hours, the highest pumping speed of H_2 is about 0.65 l/scm^2, and the highest capacity of CO is about 1.89×10^{-5} mbar·L/cm^2. The lifetime is more than 20 cycles of air exposure and re-activation. Multilayer thermal coating spray have been studying and preliminary test shows that the heating temperature could reach 300 °C, and after more than 12 times reheating, the spraying layer also shows a good adhesion.

NEG coating: For the low activation temperature and high pumping speed, surface pumping capacity, the NEG coatings of TiZrV were chosen to vacuum chambers of 4th generation photo source to reach ultra-high vacuum environment and uniform pressure distribution, like MAX IV, Sirius, ESRF-EBS, and also HEPS. The NEG coating also has been employed to suppress the e-cloud of the positron ring, which can cause beam instabilities, heat loads, and pressure increases in the vacuum system.

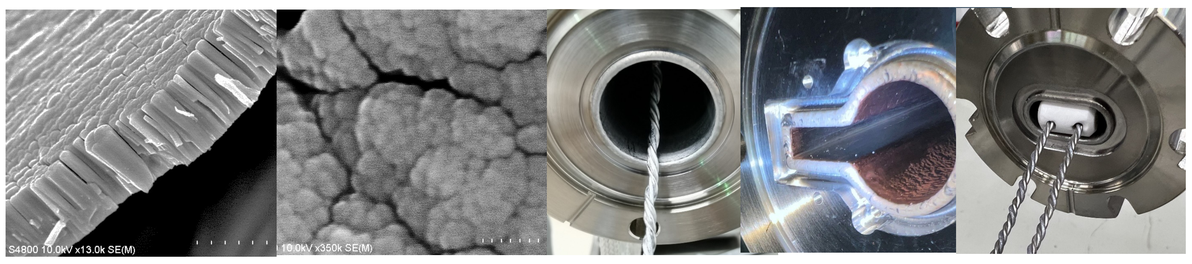

Non-evaporable getter (NEG) film coatings have been developed at IHEP to provide linear pumping for vacuum chambers of limited conductance and low SEY. Prototypes and massive production facilities were developed. The cathode is made by twisting wires of high-purity (99.95%) titanium, vanadium and zirconium each of 1 mm diameter. The solenoid is powered by a DC power supply, providing a desired magnetic field about 300 G. Film composition, the activation temperature and pumping properties have been investigated in order to optimize the deposition parameters for vacuum applications.

Prototype of NEG coating facility

Massive production facilities of NEG coating

The coating device A: Vacuum chambers are connected in parallel to 6 groups, each group of vacuum chambers length should be lower than 3.5m, outer diameter is about 0.47m; A lot of test vacuum chambers have been coated, which shows that NEG film has good adhesion and thickness distribution.

Thermal coating spraying: The baking is the most crucial procedure in achieving ultra-high vacuum. Due to NEG coating reactivation and degassing, to meet the ultra-high vacuum requirement of achieving a dynamic vacuum level of ~10^{-10} mbar. Multilayer thermal coating will be coated outside of the vacuum chamber which composited by ceramic and conductivity layer, the heating temperature could reach 300°C.

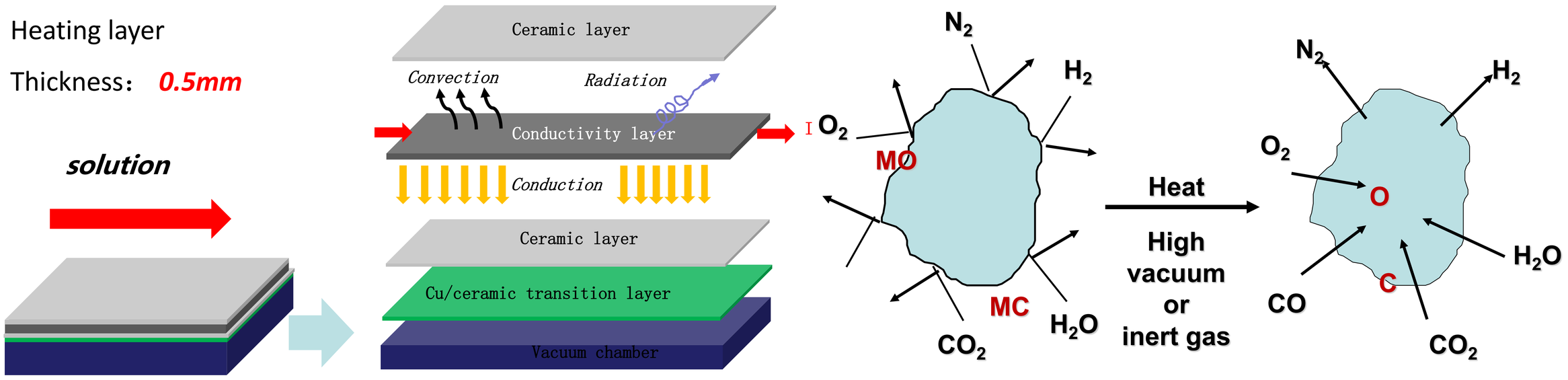

Multilayer thermal coating outside of vacuum chamber

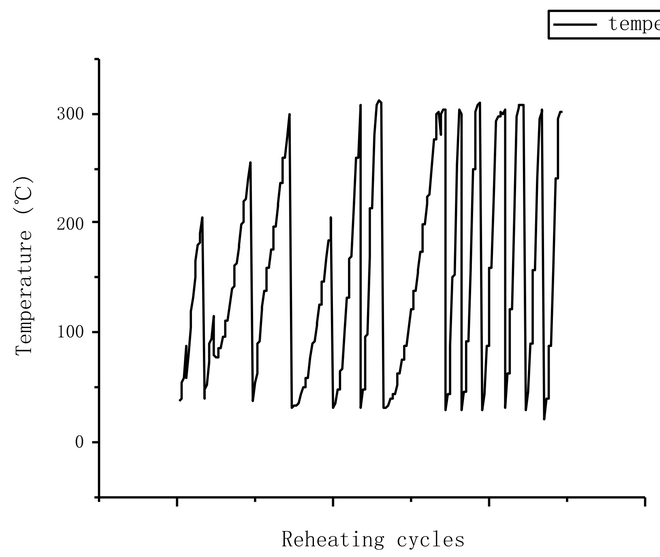

Reheating test more than 12 times

* Email: mays@ihep.ac.cn

Poster ID :400 The 2025 International Workshop on the High Energy Circular Electron Positron Collider (CEPC2025), GuangZhou, China, Nov 5-10, 2025

Alternative Solution of RF Region Beam Separating System in CEPC

B15

Guanjian Wu[1,3], Jinhui Chen[1,2], Fengli Long[1,2], Lei Wang[1,2], Lihua Huo[1], Guanwen Wang[1,2], Peng Liu[1], Chao Han[1,2], Pengfei Wei[1], Yiwei Wang[1], Fucheng Wei[1,2]

[1]Institute of High Energy Physics, Chinese Academy of Sciences, Beijing 100049, China

[2]University of Chinese Academy of Sciences, Beijing 100049, China

[3]Spallation Neutron Source Science Center, Dongguan 523803, China

中国科学院高能物理研究所 Institute of High Energy Physics Chinese Academy of Sciences

Abstract

This paper proposes kicker magnet scheme as an alternative solution of RF region beam separating system in CEPC. Two types of kicker magnet systems—resonant kicker and square wave kicker have been designed and developed. Magnetic, electrical, and thermal performance have been validated through multiphysics simulation and experiments. The vacuum and mechanical structures have been designed to ensure reliable system operation.

Introduction

In the Technical Design Report of CEPC, RF region beam separating system adopts static-electrical separator scheme, which will face challenges such as DC high voltage and beam impedance issues. In Higgs mode，e-/e+ beams only fill half ring respectively. So, it is possible to separate beams by kickers. Compared with static-electrical separator, kicker magnet is stronger and contributes lower beam impedance. Four sets of kicker locate at both sides of RF region, K1 and k4 applied for e+ beam, K2 and K3 applied for e- beam.

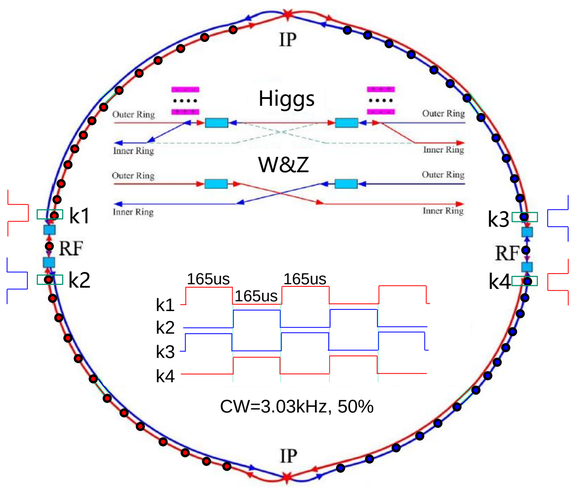

Figure1 Layout of Beam Separating System

Purpose

The waveform of kicker pulse is square wave with duty cycle of 50%, pulse width of 165 us and frequency of 3.03kHz. When resonant discharge circuit with higher efficiency and recoverable energy is adopted, the repetition frequency is 1.5MHz.

Table1 Requirements of Kicker Magnet System

Item	Value	Unit
Name	Kicker	-
Integrated strength BL	0.1624	T·m
Magnetic strength	203	Gauss
Effective magnetic length	8	m
Repetition frequency	3030	Hz
Beam clear region H×V	20.2×7.6	mm
Good field region H×V	19.2×7.2	mm

Resonant Kicker System

Two circuit modes have been designed for the resonant kicker magnet system. The fully resonant kicker magnet system is powered by two resonant power supplies. The single resonant kicker magnet system is powered by a DC power supply and generates resonant pulses through rapid switching. In resonant mode, the structural design outside vacuum will generate extremely high eddy current losses on vacuum chamber. Therefore, the structural design in the vacuum is adopted. Figures 4 and 5 show the magnetic field models of two types of kicker magnets in vacuum. Figures 6 and 7 show the circuit model designs of the kicker magnet system for two types of resonant discharge circuits.

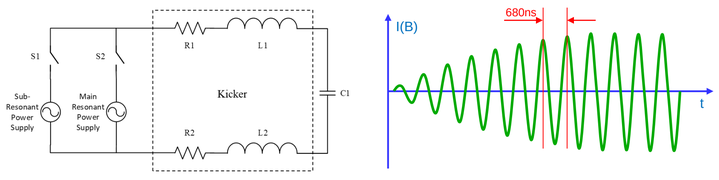

Figure2 Fully Resonant Kicker Magnet System

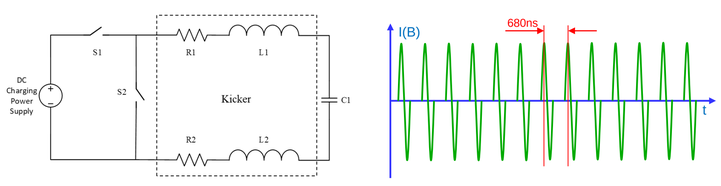

Figure3 Single Resonant Kicker Magnet System

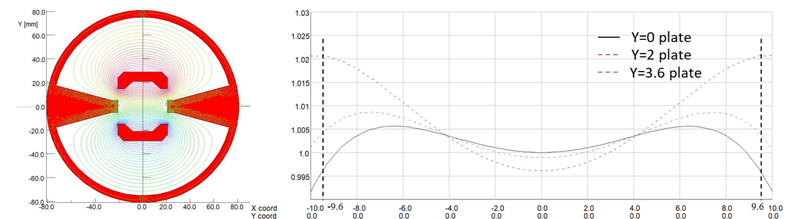

Figure4 Air-core Coil Type Kicker Magnetic Model

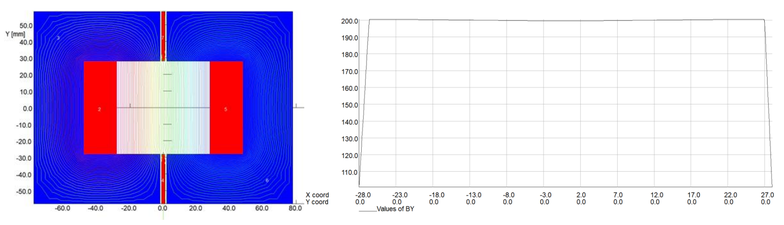

Figure5 Ferrite Type Kicker Magnetic Model

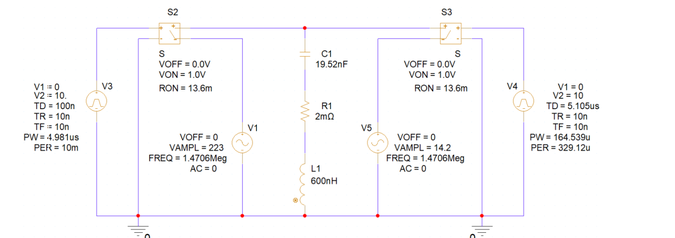

Figure6 Circuit Model of Fully Resonant Kicker System

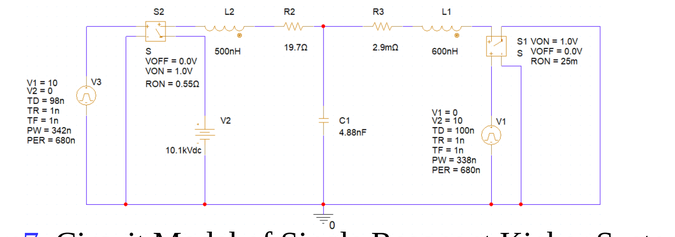

Figure7 Circuit Model of Single Resonant Kicker System

Square Wave Kicker System

Two circuit modes of square wave kicker magnet systems have been designed. One scheme is to directly generate square wave by a square wave pulse generator, which has relatively high requirements for the power supply. Another scheme is to use a DC power supply and generate square wave by switching the switches on the two branches. Figure 9 shows the circuit model of the second square wave kicker system mode.

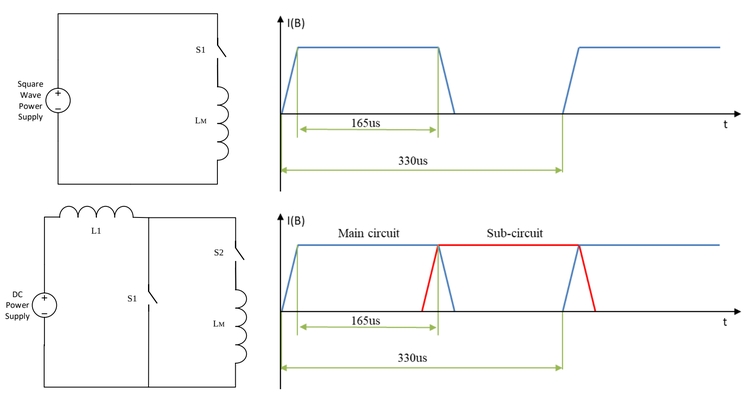

Figure8 Square Wave Kicker Magnet System

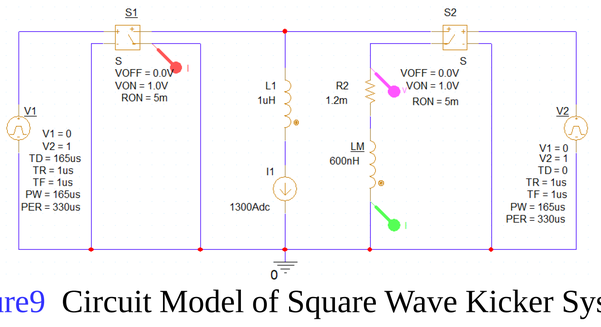

Figure9 Circuit Model of Square Wave Kicker System

The feasibility of generating square waves by switching branches of a DC power supply was experimentally validated. The kicker magnet adopts outside vacuum structure design. Vacuum chambers with metal and ceramic coating are designed and calculated. Simulation of magnetic field, eddy current loss and beam loss calculation, temperature rise calculation, and mechanical structure design were conducted in sequence.

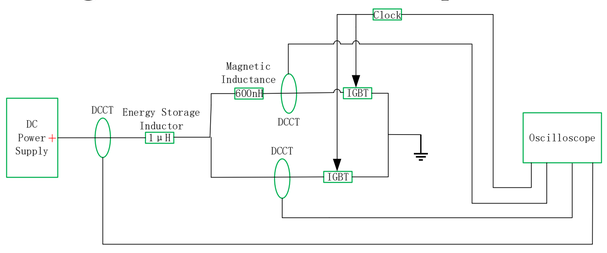

Figure10 Principle of Square Wave Circuit Test

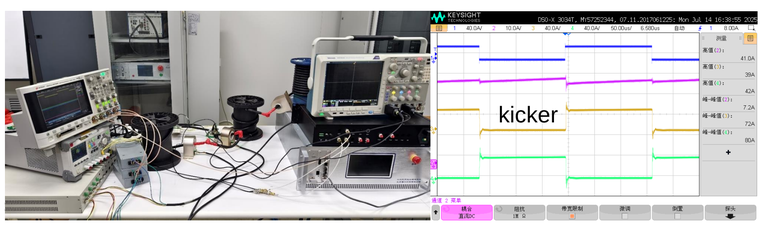

Figure11 Circuit Experiment Platform and Result

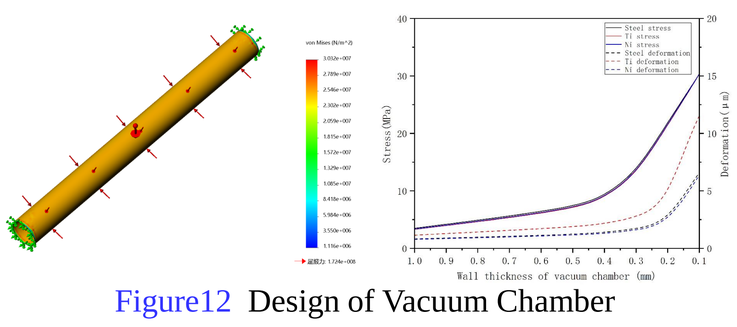

Figure12 Design of Vacuum Chamber

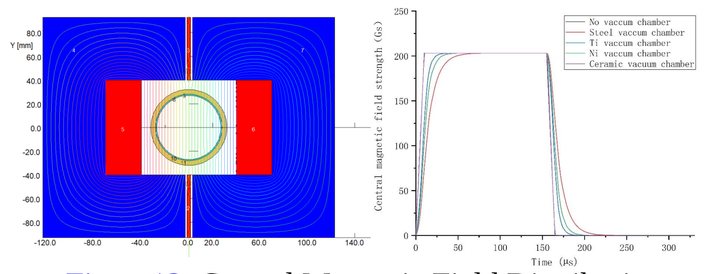

Figure13 Central Magnetic Field Distribution

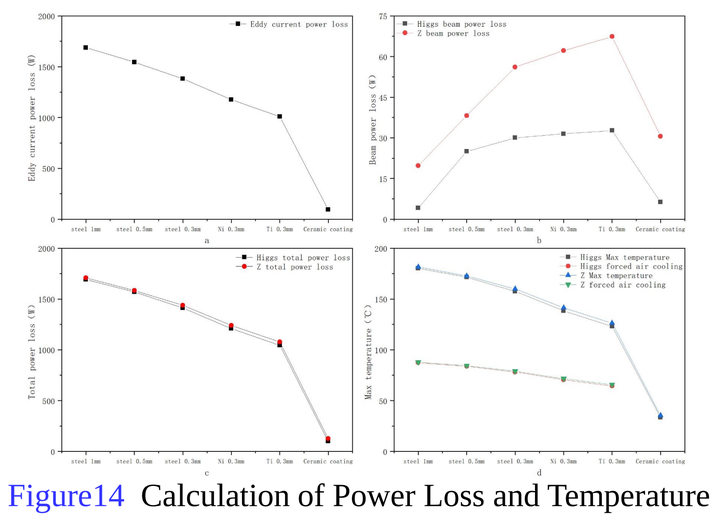

Figure14 Calculation of Power Loss and Temperature

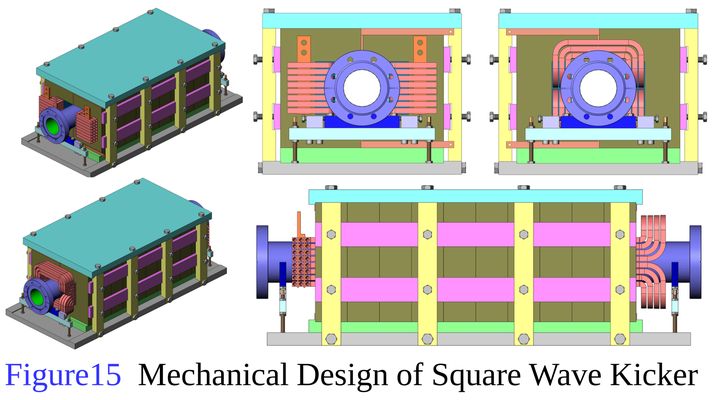

Figure15 Mechanical Design of Square Wave Kicker

Summary

This paper has completed the system design of resonant kicker and square wave kicker. The detailed circuit, magnetic field, vacuum and mechanical design of the square wave kicker have all been completed and presented. The processing and assembly of the prototype will be carried out next.

† email address: chenjh@ihep.ac.cn; wuguanjian@ihep.ac.cn